Understanding Fluorescent Protein Photoconversion and Assembly of Spinach Rubisco

Activase

by

Isabella Breen

A Thesis Presented in Partial Fulfillment
of the Requirements for the Degree
Master of Science

Approved November 2020 by the
Graduate Supervisory Committee:

Rebekka Wachter, Co-Chair
Po-Lin Chiu, Co-Chair
Marcia Levitus
Jeremy Mills

ARIZONA STATE UNIVERSITY

December 2020

ABSTRACT

Proteins function as molecular machines which perform a diverse set of essential jobs. To use these proteins as tools and manipulate them with directed engineering, a deeper understanding of their function and regulation is needed. In the studies presented here, the chemical mechanism of a fluorescent protein and the assembly behavior of a chemo-mechanical protein were explored to better understand their operation. In the first study a photoconvertible fluorescent protein (pcFP) was examined which undergoes a photochemical transformation upon irradiation with blue light resulting in an emission wavelength change from green to red. Photo-transformable proteins have been used in high resolution, subcellular biological imaging techniques, and desires to engineer them have prompted investigations into the mechanism of catalysis in pcFPs. Here, a Kinetic Isotope Effect was measured to determine the rate-limiting step of green-to-red photoconversion in the reconstructed Least Evolved Ancestor (LEA) protein. The results provide insight on the process of photoconversion and evidence for the formation of a long-lived intermediate. The second study presented here focuses on the AAA+ protein Rubisco activase (Rca), which plays a critical role in the removal of inhibitors from the carbon-dioxide fixing enzyme Rubisco. Efforts to engineer Rubisco and Rca can be guided by a deeper understanding of their structure and interactions. The structure of higher plant Rca from spinach, and its interactions with its cognate Rubisco, were investigated through negative-stain electron microscopy (EM) and cryo-EM experiments. Multiple types of higher-order oligomers of plant Rca were imaged which have never been structurally characterized, and the AAA+ core of plant Rca was shown to bind Rubisco side-on, similar to bacterial Rca's. Higher resolution structures of these

i

aggregates and complexes are needed to make definitive observations on protein-protein interactions. However, the results presented here provide evidence for the formation of regulatory structures and an experimental foundation for future exploration of plant Rca through cryo-EM.

TABLE OF CONTENTS

LIST OF TABLES

LIST OF FIGURES

LIST OF SCHEMES

CHAPTER 1

A KINETIC ISOTOPE EFFECT IN PHOTOCONVERTIBLE FLUORESCENT

PROTEIN

Abstract:

Since its discovery in 1961, the self-folding Green Fluorescent Protein (GFP) and

related proteins have been employed in numerous applications in the fields of biology,

medicine, and technology. Subsequently, the use of various fluorescent proteins as tags in

detection and imaging techniques has exploded within biological research. One such class

of these versatile proteins are the photoconvertible fluorescent proteins (pcFPs),

homologs of GFP that undergo photochemical transformation upon irradiation with blue

light, resulting in an emission wavelength change from green to red. Discovery of the

green-to-red pcFP Kaede in 2002 opened the door to the discovery of a variety of green,

red, and green-to-red fluorescent proteins expressed by stony corals. Photo-transformable

tags have since been used in high resolution, subcellular biological imaging techniques,

and desires to engineer them have prompted investigations into the mechanism of

catalysis in pcFPs. While the evolutionary trajectory of fluorescent proteins has been

deeply explored, there are significant knowledge gaps in the stepwise events of

photoconversion in Kaede-type pcFPs. Investigation of the chemical reaction has been

limited due to the flexibility of the chromophore and the high speed of the reaction,

prompting the use of amino acid replacement to evaluate the function of specific residues

and atoms in photoconversion. A comparison of pH-controlled photoconversion of the

pcFP Least Evolved Ancestor (LEA) and a mutant containing C_β-perdeuterated histidine

provides insights into the local chemical environment of the chromophore and temporal

steps of the photoconversion mechanism. Evidence for a long-lasting intermediate is observed, and significantly lower rates of photoconversion in the isotopic protein provide evidence for a rate limiting step involving the abstraction of a proton from a carbon acid at the heart of the chromophore.

Introduction:

Green-to-red photoconvertible fluorescent proteins (pcFPs) were first discovered as natural products expressed in multiple clades of the order Scleractinia, or stony corals. pcFPs spontaneously form a green chromophore once expressed and undergo a further internal transformation process when exposed to UV light, resulting in the extension of the chromophore and lengthened fluorescence emission wavelength to emit an orange or red color. Consequently, they have been presented as a powerful tool for in vivo biological imaging and detection techniques. They can be easily expressed as a tag on proteins of interest, allowing for targetable "highlighting" of specific molecules in live cells where minimal disturbance to natural processes is desired [1]. In addition, the longer emission wavelengths of their red-shifted forms are a desirable trait in fluorescent markers, as they are minimally absorbed by biological chromophores, membranes and water, and offer further penetration than visible or UV light in biological specimens [2].

Multiple genetically engineered variants of photoconvertible fluorescent proteins have therefore been optimized to serve a variety of imaging and detection purposes. pcFPs have shown promise in super-resolution microscopy techniques, including photo-activated localization microscopy (PALM) and stochastic optical reconstruction microscopy (STORM) [3,4,5]. They have also been modified for bimolecular fluorescence complementation, allowing them to act as indicators for various biological events, such as changes in cell membrane potential [6,7]. A deeper understanding of photoconversion chemistry is desired for targeted genetic engineering of these versatile proteins. However, the detailed process of pcFP catalysis has remained largely elusive, as the sequence of events and the identity of intermediates have been difficult to pin down.

To address questions about the evolution of pcFPs, the phylogenetics of fluorescent proteins of the phylum Cnidaria have been thoroughly investigated [8,9,10]. The cyan, green, and red FPs expressed by the great star coral *Montastraea cavernosa* in the order *Scleractinia* (suborder *Faviina*) indicate divergent evolution from a common green ancestor, which has been termed ALL-GFP. Amino acid differences between ALL-GFP and the extant red FPs expressed by *M. cavernosa* (all of which are Kaede-type pcFPs) were examined in order to discover key mutations responsible for the mechanistic divergence of the proteins [8]. A transitional library of possible intermediate variants was synthesized, expressed, and tested for photoconversion function before conducting a statistical analysis to determine which sites were necessary for photoconversion [10]. 13 amino acid mutations were thus discovered and applied to ALL-GFP to create the pcFP Least Evolved Ancestor (LEA), which has subsequently been used to study photoconversion kinetics and ultra-fast motions within the chromophore [10, 11, 12, 13]. Because of LEA's sensitivity to pH, bulky tetrameric structure, and relatively low quantum yield, the protein is not appropriate for use in advanced biological imaging techniques. However, delineating the photoconversion mechanism of this model pcFP may illuminate sources of pcFP efficiency and stability that can be exploited through FP engineering.

Crystal structures of LEA, combined with pH-dependent kinetic studies, have guided multiple proposed mechanisms of the photoconversion reaction. In Kaede-type proteins, the conjugated pi system of the two-ring green chromophore must extend to include a histidine in position 62 (Kaede numbering; 65 in GFP) to adopt its red fluorescent form. A series of chemical reactions are required to complete this extension,

4

which results in a β-carbon deprotonation of His62 leading to the formation of a $C_\alpha = C_\beta$ bond and a main chain bond scission between the α-carbon of His62 and the amide group of Phe61 (Scheme 1.1). Possible intermediate motions include chromophore twisting around the bonds connecting the phenol moiety to the remainder of the chromophore and twisting around the His62 α-β bond [13]. The charge of the surrounding amino acid side chains has been proposed to determine the rate of photoconversion, with the maximum rate achieved near pH 6 [11]. This rate maximum has been tentatively attributed to the pKa values of Glu211 and His193, which maintain a charged state at pH 6 that may stabilize the green chromophore, and when disrupted may trigger the photoconversion reaction. Light has been proposed to provide the energy needed to twist the phenolic end of the chromophore and block the stabilizing interaction between Glu211 and His193, allowing Glu211 to extract a proton from the β-carbon of His62. This would then allow a subsequent proton relay amongst the surrounding molecules resulting in formation of the red chromophore.
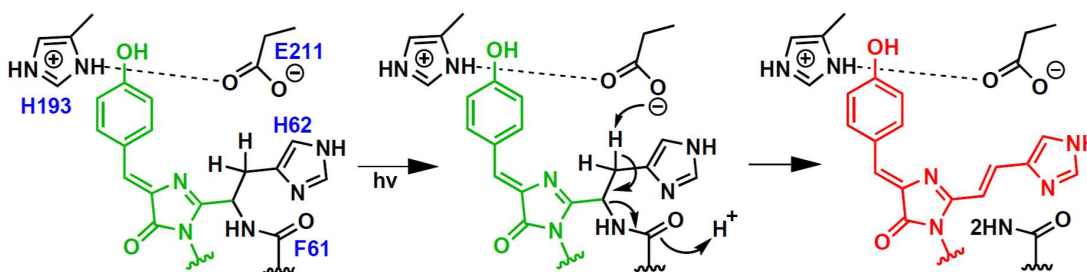
Scheme 1.1. Proposed mechanism of photoconversion in LEA, proposed by Kim et al. 2015 [11].

We propose that the photoconversion reaction of LEA is rate-limited (on the seconds-to-minutes timescale) by the slow abstraction of a proton from the His62 β-carbon during the reaction sequence. To investigate whether proton abstraction

5

determines reaction rate in green-to-red photoconvertible fluorescent proteins, we have replaced the histidine of residue 62 in LEA with C_β-perdeuterated histidine using minimal media isotopic replacement and studied the progression of photoconversion using UV-Vis absorbance spectroscopy. Proteins were diluted into several different pH conditions before photoconverting with 405 nm light during a ten-minute irradiation period. Aliquots of photoconverted protein were removed for base dilution to generate the anionic forms of the green and red chromophores before the collection of absorbance scans. Peak values attributed to the green and red chromophores were then converted to the fraction of total chromophore present and graphed as a function of time. Data was then fit to integrated first-order reaction rate equations to extract kinetic constants (min^{-1}) for green decay and red growth.

An initial fast phase of green decay, most prominent at low pH values, was recorded for both WT and isotopic LEA in accordance with previously published results [11,13]. We found that the photoconversion rate of C_β-perdeuterated histidine LEA was significantly decreased from WT with an isotope effect (k_H/k_D) ranging from ~3-5 depending on pH, with a peak kinetic isotope effect (KIE) calculated at pH 7. The high values of the isotope effect suggest an attribution to a bond-breaking event, which we assign to proton abstraction on the β-carbon of His62. The significant deceleration of photoconversion also indicates that the rate-limiting step of photoconversion was slowed down through this isotopic substitution. Based on these results, we propose that C-H bond cleavage occurs in the transition state of the major rate-limiting step in the green-to-red photoconversion process of LEA, and likely all other green-to-red pcFPs.

Materials and Methods:

      Plasmid Construction. LEA was inserted between XbaI and EcoRI sites of the pET28a+ expression vector, with a 6xHis-tag on the C-terminus. Synthesis of the protein-encoding region and insertion into the vector was performed by BlueHeron Biotechnologies. The sequence of the resultant plasmid (pET-28a(+)-LEA) was verified at the DNA Shared Resource Facility at Arizona State University.

      Protein Sample Preparation. *Expression and Purification of Wild-Type LEA.* All growth and purification procedures were performed in the dark as much as possible. Chemically competent BL21(DE3) *E. coli* were heat shocked with 50 ng/μl pET-28a(+)-LEA before selection on 100 μg/ml Kanamycin LB agar plates. 6 L of liquid LB media containing 100 μg/ml Kanamycin were inoculated with single colonies and shaken at 300 rpm and 37°C until the culture reached exponential growth (OD_{600} of ~0.6), after which IPTG was added to a final concentration of 1 mM. Expression was allowed to proceed in the dark at 25°C and 200 rpm for 17 hours. Cells were then harvested by centrifugation at 4°C and solubilized in a solution of 50 mM HEPES-NaOH pH 7.9, 20 mM Imidazole pH 7.9, 30% glycerol, 150 mM NaCl, and 0.1mM EDTA pH 7.9. The protein slurry was sonicated and then centrifuged at 4°C. The supernatant was collected and filtered through 1.2 μm filters before being applied to a HisTrap HP nickel-nitrilotriacetic acid (Ni-NTA) column (GE Healthcare) using the ÄKTA pure FPLC system. A gradient of 50 mM to 500 mM Imidazole was applied to the column, and LEA was eluted between 164 and 500 mM Imidazole concentration. Protein was pooled and dialyzed overnight against 20 mM HEPES pH 7.9, 150 mM NaCl, and 1 mM EDTA pH 7.9. Final protein concentration

was determined from A280 absorbance (ε=28880 M^{-1}cm^{-1}) before flash freezing in liquid nitrogen and storage at -80°C.

Expression and Purification of Perdeuterated Histidine Enriched LEA. Minimal media was used to express perdeuterated-histidine-enriched LEA as described previously for isotopic Tyrosine insertion [14]. A trace elements stock solution was made by adding 0.60 g of $CaCl2 \cdot 2H2O$, 0.60 g of $FeSO4 \cdot 7H2O$, 0.115 g of $MnCl2 \cdot 4H2O$, 0.08 g of $CoCl2 \cdot 6H2O$, 0.07 g of $ZnSO4 \cdot 7H2O$, 0.03 g of $CuCl2 \cdot 2H2O$, 0.002 g of $H3BO3$, 0.025 g of $(NH4)6Mo7O24 \cdot 4H2O$, and 0.50 g of EDTA-Na2 in a 100 ml solution and filter sterilizing with a 0.2-micron filter. A 100 ml 5x Minimal salts stock solution containing 3 g of $KH2PO4$, 11.32 g of $Na2HPO4 \cdot 7H2O$, 0.5 g of NaCl, and 1.0 g of $NH4Cl$ was adjusted to pH 7.2 with KOH before autoclaving at 120°C for 1 hour. A 500 ml 2x amino acid stock solution (without histidine) containing 500 mg of alanine, 400 mg of arginine, 400 mg of aspartic acid, 50 mg of cysteine, 400 mg of glutamine, 650 mg of glutamic acid, 170 mg of tyrosine, 230 mg of isoleucine, 420 mg of lysine·HCl, 250 mg of methionine, 130 mg of phenylalanine, 100 mg of proline, 2.1 g of serine, 230 mg of threonine, 230 mg of valine, 550 mg of glycine, and 230 mg of leucine was prepared and autoclaved at 120°C for 40 minutes. A 10 mg/ml solution of tryptophan and a 10 mM solution of uracil were prepared in 50 mM HEPES·NaOH pH 7.9, 300 mM NaCl solution and filter sterilized using a 0.2-micron filter. 20% glucose and 20 mg/ml thiamine solutions were prepared in deionized water and filtered through a 0.2-micron filter. A 1 M $MgCl2 \cdot 6H2O$ solution was prepared in deionized water and heat sterilized for 1 hour at 120°C. 1 L of minimal medium was prepared by combining 5 ml of the trace elements stock solution, 200 ml of the 5x minimal salts stock solution, 500 ml of the 2x amino acid

stock solution, 25 ml of the tryptophan stock solution, 20 ml of the uracil stock solution, 20 ml of the glucose stock solution, 2 ml of the thiamine stock solution, 1 ml of the MgCl2 stock solution, and deionized water.

1000 µl of Kanamycin and 100 mg perdeuterated Histidine (Cambridge Isotopes Laboratories, Catalog #DLM-7855-0) was added to the 1 L of minimal medium immediately prior to inoculation with a single colony of BL21(DE3) pET-28a(+)-LEA. The culture was grown at 37°C while being shaken continuously at 300 rpm. Upon entering the exponential growth phase, the culture was induced with IPTG and provided 5 ml of 20% glucose. The temperature and shaker speed were reduced to 25°C and 200 rpm for 17 hours. The pellet was harvested, purified, and stored as described for WT LEA above.

Mass Spectrometry Analysis of Products. Protein samples were mixed at a 1:1 concentration with sinapinic acid matrix (50% acetonitrile and 0.1% trifluoroacetic acid) and subjected to Matrix-Assisted Laser Desorption/Ionization Time-of-Flight (MALDI-TOF) in the AB SCIEX 4800 MALDI TOF/TOF MS located at the Mass Spectrometry Facility at Arizona State University. The procedure was performed by Isabella Breen. Three separate mass analyses were performed for both WT LEA and perdeuterated Histidine Enriched LEA. Electrospray-ionization mass spectrometry of both proteins was performed by Julian Whitelegge (UCLA).

LED Light Box Specifications. Tight-tolerance UV LED lamps (BIVAR) emitting 405 ± 2.5 nm light with a 40 mW emitting power (Part # UV3TZ-405-30) and a 30° viewing angle were used to illuminate protein samples. Three LEDs were mounted immediately adjacent to each other in a home-built light box equipped with a 25 W DC

power supply and on-off switch. Sample cuvettes were placed directly adjacent to the LED light to give a path length of 1 cm. At a constant current of 10 mA, the irradiance of the LEDs at the cuvette was 54.3 ± 0.4 W/m^2, as measured with a Li-Cor LI-250 Light Meter.

Calculation of Anionic Chromophore Extinction Coefficients. The 280 nm wavelength extinction coefficient for LEA was calculated using the free online ExPASy ProtParam tool. The concentration of total protein was calculated using this coefficient according to Beer's Law, which states that absorption of light by a chemical is equal to the extinction coefficient (units M^{-1}cm^{-1}) multiplied by the molar concentration of the substance and the path length (in cm) of the sample . An extinction coefficient for the green anionic chromophore was obtained by dividing the absorbance of the anionic chromophore at 504 nm (in pH 10 buffer) by the total concentration of protein. This experiment was performed in triplicate. Absorbance spectra of the protein in partially photoconverted states were used to determine the extinction coefficient for the red chromophore. 1 ml of 0.1 mg/ml WT LEA protein was exposed to 405 nm light in a pH 7.5 buffer (50 mM HEPES, 150 mM NaCl, and 1 mM EDTA) for 30 minutes. At five-minute intervals, illumination was paused and 40 µl of the solution was removed for dilution into 360 µl of pH 10.0 buffer. The solution was allowed to equilibrate in the dark for 48 hours before collecting an absorbance spectrum between 250 to 650 nm. The loss in concentration of green chromophore between time points at 15, 20, 25, and 30 minutes was calculated using our experimentally determined extinction coefficient for the green anionic chromophore. Early photoconversion time points (<10 minutes) were avoided to prevent overestimation of photoconversion from accelerated green chromophore loss.

The loss in green chromophore concentration was then equated to the increase in red chromophore concentration at each time point. A clean isosbestic point at ~518 nm was observed across all time points collected, indicating a 1:1 conversion (Fig. 1.1, Panel A).The difference in absorbance of the red anionic chromophore at 571 nm was divided by the green chromophore loss concentration for each five-minute interval, and the resultant values were averaged to obtain the working anionic red chromophore extinction coefficient.

Photoconversion of Wild-Type and Isotopic LEA. Photoconversion was performed at room temperature in the LED light box (See Methods) which prevented ambient light from illuminating the sample. Absorption spectroscopy was performed using a Shimadzu UV-2401 spectrophotometer at room temperature. Protein was diluted to 1 mg/ml concentration in 1 ml of a pH-controlled buffer. 10 separate pH conditions were tested (pH 4.5, 5.0, 5.52, 6.04, 6.47, 7.0, 7.48, 8.01, 8.51, and 9.0). Buffers contained 50 mM Acetate, Citrate, Bis-Tris, HEPES, CHES, or Tris, 100 mM NaCl, and 0.1 mM EDTA. 1 ml protein solutions were exposed to 405 nm light for 1, 3, 5, 7, 10, 15, 20, 25, and 30 total minutes. Illumination was paused at each time point by switching off the LED apparatus and 40 µl of the protein solution was removed for 10x dilution into 360 µl of high pH buffer (100 mM CHES pH 10.00, 100 mM NaCl, 0.1 mM EDTA). After 48 hours of equilibration at room temperature in the dark, absorbance scans (250-650 nm) of the base-diluted samples were collected. Three trials were performed at each pH value for both LEA and C_β-perdeuterated histidine LEA.

Modeling Kinetics of Photoconversion in Wild-Type and Isotopic LEA.
Photoconversion data for WT and isotopic LEA was evaluated to quantify total and

relative amounts of red and green chromophore at each time point for each pH condition. Absorption values at 504 and 571 nm were converted to green and red LEA concentrations using experimentally determined extinction coefficients (88708 $M^{-1}cm^{-1}$ and 91324 $M^{-1}cm^{-1}$, respectively). Concentrations of both chromophore types were normalized to the highest concentration of green chromophore throughout the experiment, referred to as total chromophore concentration. We then used scipy.optimize.curve_fit to perform a non-linear least squares regression to fit integrated first-order reaction rate law equations to the change in total green and red chromophore over time and calculate one standard deviation error on the parameters. Single and double exponential integrated first-order reaction rate equations were then fit to the data. All red growth data and green decay data was fit to eq 1 and eq 2,

$$A = 1 - e^{-k_s t} \qquad (1)$$
$$A = e^{-k_s t} \qquad (2)$$

describing single exponential growth and decay, respectively. The only exception to this was green chromophore decay at low pH (4.5-5.0 or 5.5) for both WT and C_β-Deuterated Histidine LEA, which was modeled with two kinetic rate constants by eq 3

$$A = A_1 \cdot e^{-k_s t} + (1 - A_1) \cdot e^{-k_f t} \qquad (3)$$

to account for a change in decay rate after ~1-2 minutes of light exposure. The secondary slower phase rate (k_s) was used to represent the green decay rate in calculations, because

12

the majority of the chromophore decays at this secondary rate. In equations 1, 2 and 3, A is the fraction of total chromophore, A_1 refers to the fraction of total chromophore proceeding at the attached kinetic rate, k_s and k_f refer to the fast and slow kinetic rates, respectively, in fraction of chromophore/minute, and t refers to time in minutes. A kinetic isotope effect (k_{sH}/k_{sD}) was calculated at each pH condition with errors propagated from the extracted kinetic rates.

      Prolonged dark-adaptation of WT LEA after photoconversion. WT LEA was tested for the stability of the relative amounts of green and red chromophores after illumination, as a prolonged dark-adaptation step leading to an increase in red chromophore has been recorded in the past [15]. Absorbance scans of the protein were taken after photoconversion at pH 5.5, either immediately following light exposure or after 48 hours of incubation in the dark in pH 5.5 or pH 10 buffers. Protein was diluted to a 0.1 mg/ml concentration in 50 mM acetate pH 5.5, 100 mM NaCl, and 0.1 mM EDTA buffer solution. The solution was exposed to 405 nm LED lights for 10 minutes. A 40 µl aliquot was removed and diluted 10-fold into a buffer at pH 10 containing 100 mM CHES, 100 mM NaCl, and 0.1 mM EDTA before either taking an absorbance scan or placing in the dark at room temperature for 48 hours. An additional 40 µl aliquot was kept in the dark for an equal amount of time without dilution into base. After the 48-hour waiting period, this sample was diluted into base immediately before taking an absorbance scan. Relative levels of green and red chromophore were compared from each absorbance scan to determine whether the apparent increase in red anionic absorbance over the 48-hour waiting period was due to base equilibration or additional processes.

Results:

Incorporation of C$_\beta$-perdeuterated Histidine into LEA. To evaluate the significance of C-H bond cleavage on the rate of photoconversion, we performed isotopic residue replacement on the green-to-red pcFP LEA. LEA was grown in minimal media containing all canonical amino acids except for histidine, which was replaced with C$_\beta$-perdeuterated histidine for global incorporation of the isotopic residue. Growth of the WT protein in the same minimal media with natural histidine incorporated resulted in overexpression of WT LEA, with no discernible differences from LB media-grown WT LEA. Two 6 L cultures of BL21(DE3) pET2(a+)-LEA grown in liquid LB media yielded a total of 756 mg of purified WT LEA protein. Purification of WT LEA and C$_\beta$-perdeuterated Histidine LEA in minimal media yielded 195.4 mg/L and 211 mg/L, respectively. C$_\beta$-perdeuterated histidine LEA and WT LEA were compared via mass spectrometry analysis. The expected mass of LEA is 26412 Da, and an increase of 75 Da is expected from complete incorporation of isotopic histidine into every Histidine position on the protein. The average masses measured by MALDI-TOF for LEA and perdeuterated Histidine LEA were 26418 ± 39 Da and 26516 ± 46 Da, respectively, with a mass difference of 98 ± 60 Da. A 74-Da difference was measured between WT LEA and perdeuterated Histidine LEA (26265 Da and 26339 Da, respectively) using intact mass spectrometry (Julian Whitelegge, UCLA). The measured mass of each protein was smaller by roughly ~150 Da each, possibly caused by loss of an N-terminal methionine residue. The mass difference was consistent with complete incorporation of C$_\beta$-perdeuterated histidine into each histidine position in LEA.

Continued Increase of Red Chromophore Following UV Illumination. The relative abundance of green and red chromophore was monitored after photoconversion over a 48-hour period to determine if additional processes were occurring in the dark with and without a base-dilution step. A sample at 0.1 mg/ml concentration in pH 5.5 buffer was photoconverted before being kept in the dark for 48 hours at the same pH or diluted
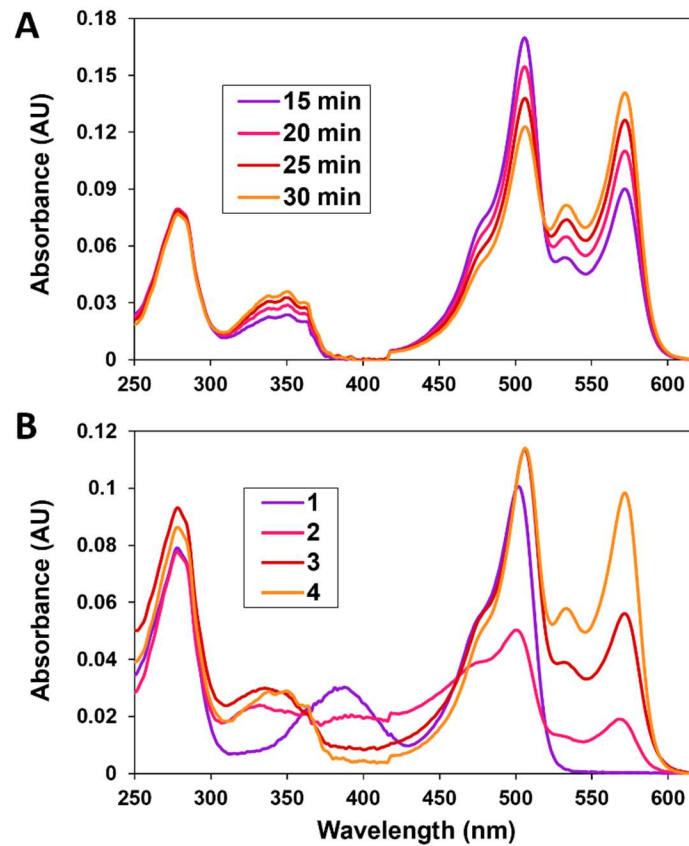
Figure 1.1 (A) Absorbance spectra of LEA throughout photoconversion at pH 7.5. Spectra at each time point (15, 20, 25, and 30 minutes) were taken after photoconversion, base dilution, and 48 hour in-the-dark equilibration. A clear isosbestic point can be seen between 518-519 nm, indicating quantitative conversion from the green to red species. (B) Absorbance spectra of LEA before and after photoconversion, with and without base dilution. Spectrum 1 is of LEA diluted to 0.1 mg/ml at pH 5.5; 2 is of LEA photoconverted at pH 5.5 for ten minutes; 3 is of LEA photoconverted at pH 5.5 for ten minutes and diluted into pH 10 buffer; 4 is of LEA photoconverted at pH 5.5 for ten minutes, equilibrated in the dark for 48 hours, and subsequently diluted into pH 10 buffer.

10-fold into pH 10 buffer. Resultant absorbance scans are shown in Fig. 1.1, Panel B.

Absorbance peaks at 386 nm and 504 nm indicate the neutral and anionic green

chromophore, respectively. Spectra (1) and (2) highlight the apparent decrease in green

chromophore absorbance and increase in red chromophore absorbance after 10 minutes

of photoconversion at pH 5.5. A decrease in neutral and anionic green chromophore is

observed, and an increase in red anionic chromophore can be seen at 571 nm. Absorption

of the neutral red chromophore (460 nm) is obscured by the tail of the green anionic

chromophore. When LEA is photoconverted at pH 5.5 for ten minutes and immediately

diluted into pH 10 base, the neutral forms of the chromophores are deprotonated, leading

to an increase of features associated with the anionic forms of the green and red

chromophores (Spectrum 3). If allowed to adapt after photoconversion in the dark before

base-dilution, as is shown in spectrum 4, a significant increase in red anionic

chromophore is observed, similar to results seen previously [15]. However, a

corresponding decrease in green chromophore is not observed, indicative of an

intermediate formed during photoconversion that completes conversion into the red

anionic form over an extended period in the dark.

A Primary Deuterium Isotope Effect for Proton Abstraction in Photoconversion.
Carbon-hydrogen bond cleavage at C_β of histidine 62 has been established as a necessary

component of the mechanism for green-to-red photoconversion. Although proton

abstraction by a nearby base has been proposed by several groups, the order of events

surrounding this step is still debated, and it remains unknown whether backbone scission

precedes or follows the formation of the double carbon bond between C_α-C_β on His62.

We measured the relative photoconversion rates of WT and isotopic LEA (containing C_β-

perdeuterated histidine) to determine whether deuteration slows the photoconversion process. A significant decrease in the photoconversion rate of deuterated LEA would indicate that proton abstraction is fully rate-limiting.

The relative abundance of green and red chromophore was monitored during photoconversion at several different pH values to compare the pH-dependence and rates of green chromophore decrease and red chromophore increase (Fig. 1.2). pH-dependence of photoconversion in LEA has been explored previously, but measurements focused on the decrease of green chromophore due to the difficulty of quantifying the red
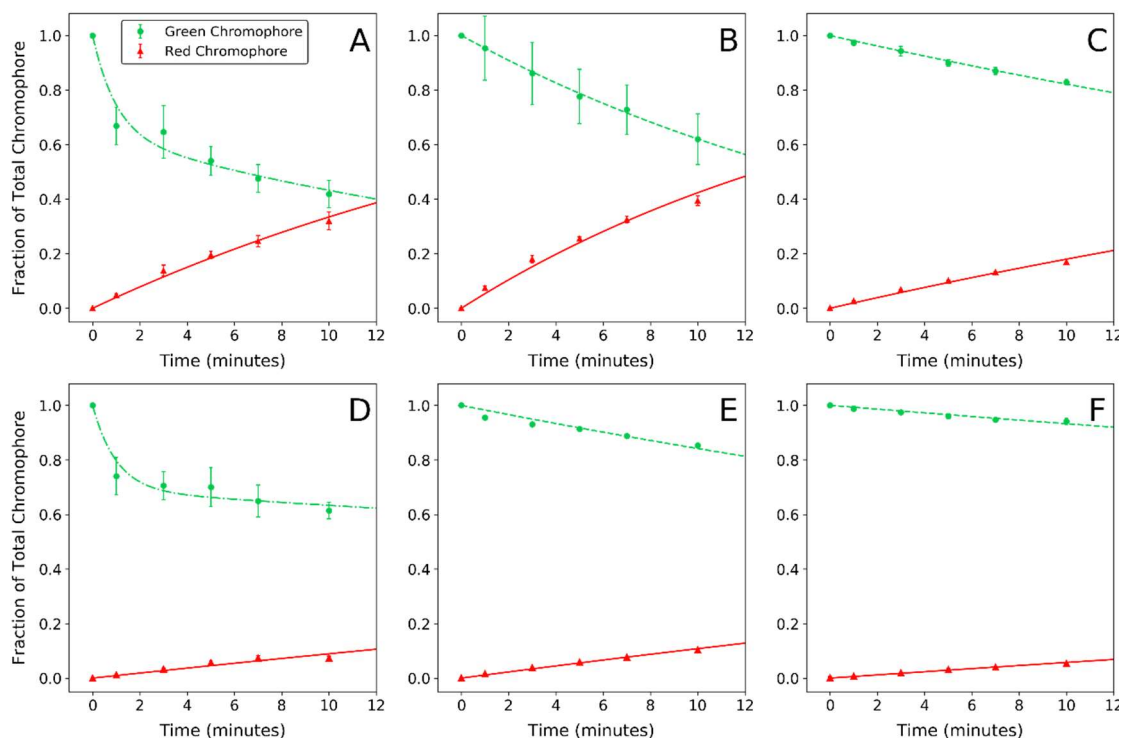
Figure 1.2. Fraction of green and red chromophore present in WT LEA (A, B, and C) and Cβ-perdeuterated Histidine LEA (D, E, and F) as a function of irradiation time at pH 4.5 (A and D), pH 7.0 (B and E) and pH 8.5 (C and F). Average fraction of total chromophore at each time point (n=3) is denoted by circles for the green chromophore and triangles for the red chromophore (see legend). Solid red lines indicate a curve fit to eq 1, dashed green lines indicate a curve fit to eq 2, and dashed and dotted green lines indicate a curve fit to eq 3.

17

chromophore over a range of pH conditions [11]. The neutral and anionic chromophores absorb at ~386 and ~504 for the green chromophore and ~460 and ~571 for the red chromophore, respectively. Because the absorbances of neutral red and anionic green chromophores are near one another, resolving the two species is difficult at or near neutral pH. During photoconversion, samples were removed and diluted into a high-pH solution to turn the entire chromophore population anionic so their absorbance peaks could be resolved, and the total amount of green and red chromophore could be measured (Fig. 1.2). A dark adaptation period was included before absorbance scan collection to ensure complete conversion to anionic chromophore, as well as to allow any post-illumination reactions to go to completion. Quantities of the total green and red chromophores were obtained using experimentally determined extinction coefficients for their anionic forms (88708 $M^{-1}cm^{-1}$ and 91324 $M^{-1}cm^{-1}$, respectively). The resultant data
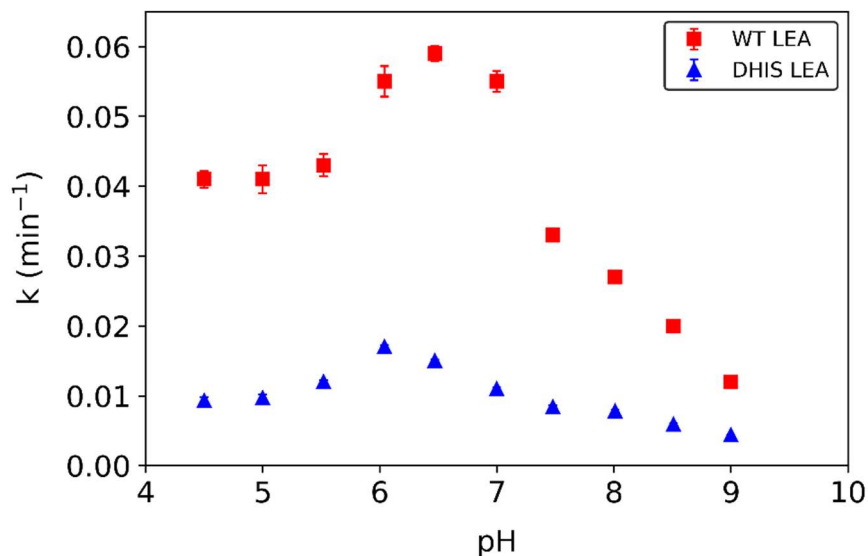
Figure 1.3. Extracted kinetic constants for red growth in WT LEA (red squares) and C_β-perdeuterated histidine LEA ("DHIS" LEA, blue triangles) across a range of pH conditions (4.5-9). The red fraction of total chromophore was tracked during irradiation by 405 nm light over the course of 10 minutes. Kinetic rate constants were extracted by fitting red chromophore growth to eq 1 and are shown here as a function of pH. Standard deviations are shown as vertical lines.

18

was graphed as a fraction of total chromophore over time and fit to the first-order reaction equations, and kinetic constants extracted. Single- or double-exponential reaction rate law equations were used as appropriate; most data were fit to single exponential equations (eq 1 and 2, panels B, C, E and F in Fig. 1.2). However, a few kinetic data sets for the loss of the green chromophore between pH 4.5-5.5 indicated a distinct fast phase (k_f) that preceded a slower phase (eq 1 and panels A and D in Fig. 1.2). For kinetic isotope effect calculations, the slower decay rate, k_s, of these fits was used as it described most of the green chromophore loss.

Table 1.1 Comparison of the rate constants for the rise of the red chromophore in WT and C_β-perdeuterated histidine LEA.

	Red Growth Rate Constant k_s (min^{-1})		
Buffer pH	**Wild Type LEA**	**Isotopic Histidine LEA**	k_H/k_D
4.50	0.0407 ± 0.0012	0.00933 ± 0.00049	4.4 ± 0.3
5.00	0.0415 ± 0.0020	0.00971 ± 0.00049	4.3 ± 0.3
5.52	0.0432 ± 0.0016	0.0124 ± 0.0002	3.5 ± 0.1
6.04	0.0550 ± 0.0022	0.0167 ± 0.0003	3.3 ± 0.1
6.47	0.0587 ± 0.0011	0.0151 ± 0.0002	3.9 ± 0.1
7.00	0.0551 ± 0.0015	0.0114 ± 0.0002	4.8 ± 0.1
7.48	0.0332 ± 0.0008	0.00840 ± 0.00025	3.9 ± 0.2
8.01	0.0275 ± 0.0007	0.00776 ± 0.00017	3.5 ± 0.1
8.51	0.0199 ± 0.0004	0.00591 ± 0.00013	3.4 ± 0.1
9.00	0.0118 ± 0.0001	0.00437 ± 0.00004	2.7 ± 0.0

Comparison of red chromophore growth and green decay rates between the two protein types was made by calculating a kinetic isotope effect or KIE (k_H/k_D) for each pH condition (Table 1.1, Table 1.2). Red chromophore growth rates were significantly slowed in C_β-deuterated histidine LEA, with KIE values ranging from 2.7 to 4.8 (Table

19

1.1; Fig. 1.3). The largest kinetic isotope effect was seen at neutral pH. The highest rates of photoconversion for each protein were recorded at pH ~6.5 for WT LEA and pH ~6.0 for C_β-deuterated histidine LEA, consistent with previously recorded results [11].

An initial fast green chromophore decay rate similar to that observed by Kim et al. occurred in the first ~2 minutes of photoconversion but appeared to only occur at low pH (Table 1.2) [11]. The slower rate (denoted k_s) had a larger relative amplitude (A1) than that of the fast rate (k_f) and was therefore used for kinetic isotope effect (k_{sH}/k_{sD}) calculations (Table 1.2). Although in this instance we could not observe relative rates of the neutral and anionic chromophores, previous studies indicate that this fast phase only affects the neutral form of the green chromophore [11,13]. The authors proposed that this loss is due primarily to photobleaching via chromophore twisting or photodamage, which is supported by recent femtosecond stimulated Raman spectroscopy data [13]. Rates

Table 1.2 Comparison of Green Decay Rates in WT and C_β-perdeuterated Histidine LEA.

	Wild Type LEA Green Decay			Isotopic Histidine LEA Green Decay			
Buffer pH	k_f (min^{-1})	k_s (min^{-1})	A_1	k_f (min^{-1})	k_s (min^{-1})	A_1	k_{sH}/k_{sD}
4.50	1.0 ± 0.5	0.039 ± 0.022	0.64 ± 0.10	1.0 ± 0.5	0.0084 ± 0.0129	0.69 ± 0.07	4.6 ± 7.6
5.0	1.0 ± 0.3	0.052 ± 0.008	0.71 ± 0.04	1.0 ± 0.9	0.025 ± 0.011	0.84 ± 0.07	2.1 ± 1.0
5.52	1.0 ± 0.8	0.062 ± 0.009	0.87 ± 0.06	*n/a*	0.017 ± 0.001	*n/a*	3.6 ± 0.6
6.04	*n/a*	0.079 ± 0.005	*n/a*	*n/a*	0.023 ± 0.003	*n/a*	3.4 ± 0.5
6.47	*n/a*	0.070 ± 0.003	*n/a*	*n/a*	0.021 ± 0.001	*n/a*	3.3 ± 0.2
7.00	*n/a*	0.048 ± 0.005	*n/a*	*n/a*	0.017 ± 0.001	*n/a*	2.8 ± 0.3
7.48	*n/a*	0.037 ± 0.002	*n/a*	*n/a*	0.021 ± 0.004	*n/a*	1.8 ± 0.3
8.01	*n/a*	0.028 ± 0.001	*n/a*	*n/a*	0.010 ± 0.001	*n/a*	2.8 ± 0.2
8.51	*n/a*	0.020 ± 0.001	*n/a*	*n/a*	0.0070 ± 0.0004	*n/a*	2.8 ± 0.2
9.00	*n/a*	0.013 ± 0.001	*n/a*	*n/a*	0.0083 ± 0.0005	*n/a*	1.6 ± 0.1

obtained for the slow phase of green loss were equal to or slightly higher than that of red rise, indicating that although multiple processes contribute to green chromophore loss, photoconversion is the main process occurring. Green decay rates were generally higher than red growth in WT LEA than in isotopic LEA, which resulted in a lower average KIE (2.9 ± 0.9) for green decay.

Discussion:

Although the discovery of novel natural pcFPs has slowed down in the last few decades, exploration of their internal chemistry shows no signs of stopping. Like GFP, green chromophore maturation in pcFPs is self-catalyzed during expression. However, these proteins also possess the ability to perform a coordinated elimination reaction and bond scission in response to UV light exposure. For this reason, pcFPs have promising applications in biological imaging techniques and are used to study processes in enzyme catalysis. Monitoring photoconversion and identifying the key components of the reaction is difficult, however, due to the fast timescale of the mechanism and the short-lived intermediates involved. Crystal structures of the proteins in their green and red states offer high-resolution "before" and "after" pictures, against which proposed mechanisms can be compared for their physical feasibility. Combined with UV-Vis/IR spectroscopy, multiple possible chromophore species involved in photoconversion have been identified. Comparisons of mutants have offered a more direct analysis of specific residue involvement and chromophore behavior in GFP-like proteins, indicating the importance of certain residues in the chromophore pocket. However, temporal information is necessary to understand and organize mechanistic steps.

We have expanded upon previously established methods to measure photoconversion rates in the green-to-red photoconvertible fluorescent protein LEA, and used these methods on a newly synthesized isotopic version of the protein, C_β-perdeuterated histidine LEA. A similar isotopic residue replacement technique was previously used to examine the GFP maturation process [14]. By limiting deuterium replacement to histidine residues, of which there is only one bonded to the chromophore, we focused our inquiry to photoconversion rate dependence on proton abstraction from the β-carbon on histidine 62. Although deuterons are also attached to carbons 2 and 5 of the imidazole ring of C_β-perdeuterated histidine, these carbon atoms cannot serve as hydrogen bond donors and the presence of these atoms should not affect the photoconversion process.

Dilution of the protein into base allowed us to measure both the decrease in green chromophore and increase in red chromophore over the course of continuous photoconversion. Fitting the data to first-order rate law equations allowed for the extraction of kinetic constants for photoconversion of WT and isotopic LEA. Comparison of the red growth rates produces a significant kinetic isotope effect (KIE = 4.8 ± 0.1) at pH 7. KIE's calculated at several different pH's between 4.5 and 9 average at 3.8 ± 0.6. The distinct delay in photoconversion of C_β-perdeuterated histidine LEA indicates a primary isotope effect, in which a deuteron-carbon bond is broken as part of a rate-limiting step, and the hydrogen is transferred in the transition state of that step

Previous studies have put forth outlines of the photoconversion mechanism in green-to-red pcFPs, which include a β-elimination reaction and bond scission to produce the red form of the protein. However, it is debated whether Kaede-type green-to-red pcFPs undergo a backbone bond scission before or after proton abstraction from C_β of His62. In

one case, loss of a proton from the phenolic hydroxyl group could allow for electron donation through the pi conjugated system to the backbone carboxyl group, which then receives a proton (possibly from N_δ on His62). Bond scission between the C_α-N_α of His62 would follow, forming a carbocation on C_α. C_β of His62 would then lose a proton and a double bond (C_α=C_β) would be formed in an E1 elimination reaction [16,17]. Alternatively, a base such as Glu212 could remove the proton from C_β of His62 and backbone scission could occur simultaneously or as a secondary step [12,18,19].

Structural analysis of the green-to-red pcFP KikGR by Tsutsui et al. supports an E1 reaction mechanism based on the cis-conformation of the double carbon bond in the (5-imidazolyl) ethenyl group in the red form [16]. In EosFP, Kaede, and LEA, the final red chromophore structures show a trans double bond between the alpha and beta carbons of histidine 62. Both outcomes are still possible with an E1 mechanism, and energetic calculations show that the E1 mechanism provides a low-energy route to photoconversion. Nienhaus et al. showed that replacing Glu212 with glutamine in EosFP abolished all photoconversion ability, providing compelling evidence that glutamate acts as a proton acceptor in an E2 beta-elimination reaction that leads to bond scission [18]. Kim et al. proposed that these mechanisms could occur simultaneously based on structures of the green and red chromophores in LEA, with bond scission being driven by proton delivery to Phe61 through a relay or shuttling mechanism [11]. Whether a part of the same concerted step or temporally separated, an E2 mechanism avoids the formation of an unstable carbocation on the alpha carbon of His62.

Taking these possibilities into account, any step of the proposed mechanisms could be restrictive on the overall rate of photoconversion. We postulated that if proton abstraction

is the rate-limiting step of photoconversion, C_β-perdeuterated His62 should significantly slow down the reaction. If the rate was limited by the main chain bond scission step or other conformational change, a significant slowdown in photoconversion would not be observed in isotopic protein. Whether the photoconversion mechanism follows a stepwise reaction or is of a concerted nature, our results show that proton abstraction from the β-carbon of Histidine 62 is fully rate-limiting.

A significant increase in red chromophore for a sustained period in the dark was observed, providing evidence that the nascent chromophore undergoes additional modifications after illumination has been stopped. We do not see a matching decrease in the green chromophore over this period. This would indicate that chromophore irradiated with 400 nm light proceeds through an intermediate state not readily identified through our spectroscopic methods which can then fully convert to the red form in the dark. The intermediate is quantitatively converted to the red form, as indicated by a clean isosbestic point in Fig. 1.1 (Panel A). Measurements of the red chromophore after photoconversion were collected after a 48-hour dark incubation, during which all intermediates were converted to the final red form. Therefore, our measurements reflect the amount of intermediate formed as a function of time, and the observed rate retardation indicates that C-H bond cleavage must occur prior to the formation of the putative intermediate.

Fare et al. provides spectroscopic evidence from EosFP of a stable intermediate which has undergone $C_\alpha = C_\beta$ histidine bond formation and backbone scission but has not formed the final red chromophore [20]. It is possible that the slow increase in red chromophore we see is populated by the same long-lived intermediate found to accumulate in low pH conditions in EosFP [20]. They propose a few possible identities

for this intermediate, but their analysis supports the formation of a green chromophore and a nearby tyrosyl radical. They observed absorption at 434 nm in time-resolved spectra during photoconversion, which they suggest is consistent with such an intermediate. Our UV-Vis spectra show an overall increase in absorption between ~410-460 nm after 10 minutes of irradiation at pH 5.5, which may be attributed to the same intermediate and/or the red protonated chromophore (abs. ~455 nm), which also populates this region of the absorption spectra [13]. In principle, it is possible that the putative intermediate constitutes a conformational precursor to the planar red chromophore. If the intermediate is a substantially distorted three-ring chromophore, which lacks coplanarity of the ring systems, the absorption would be blue-shifted from the final red form.

In this study we confirm that during early stages of UV light exposure in low pH conditions, the green chromophore experiences an increased rate of irreversible loss, which may be due to intermediate accumulation, photobleaching by deformation or reversible twisting, or a combination of the above. As identified in previous work, the sole photoconvertible species is the green neutral form of the chromophore and this initial fast phase only affects this form [11,13]. However, this species favors photoswitching over photoconversion, which may lead to the accumulation of trapped species and subsequent decline in green decay rate [13]. Although the fast decay rate constants extracted here are not completely reliable due to their reliance on ~2 data points, the fast rate is not as heavily affected by isotopic histidine replacement as the secondary slow rate. Additionally, red chromophore rise can be described by a single exponential process

for the entire dataset. Together these findings suggest the initial dip in green chromophore is due to a non-photoconversion process.

Conclusion:

In this work, C_β-Deuterated Histidine LEA was produced in minimal media through isotopic enrichment throughout expression of the WT protein. Photoconversion at low-irradiation conditions was monitored via absorbance of green and red chromophores that were brought to their anionic forms after UV light exposure through an increase in buffer pH. The resultant fractions were graphed as a function of time and fit to first-order reaction equations for extraction of a kinetic rate constant. Rate constants were then graphed as a function of pH for each protein type and compared. We observed a significant kinetic isotope effect over a range of pH conditions, suggesting that histidine C_β de-protonation is fully rate-determining and consistent with simultaneous proton transfer in the transition state of the rate-limiting step. The continuous formation of red chromophore in the dark after illumination with UV light indicates the formation of an intermediate state during illumination which has not yet been identified. However, our experimental design accounts for conversion of the intermediate into its final form, and our results confirm that C-H bond cleavage from C_β of His62 occurs before the formation of the intermediate.

References:

1.   Schmidt, A.; Wiesner, B.; Schülein, R.; Teichmann, A. Use of Kaede and Kikume Green-Red Fusions for Live Cell Imaging of G Protein-Coupled Receptors. *Methods Mol Biol* **2014**, *1174*, 139–156. https://doi.org/10.1007/978-1-4939-0944-5_9.

2.   Hilderbrand, S. A.; Weissleder, R. Near-Infrared Fluorescence: Application to in Vivo Molecular Imaging. *Curr Opin Chem Biol* **2010**, *14* (1), 71–79. https://doi.org/10.1016/j.cbpa.2009.09.029.

3.   Ma, M.; Ay, K.; Lr, S.; K, N.; Cj, O.; J, L.-S.; Gu, N.; P, P. Rational Engineering of Photoconvertible Fluorescent Proteins for Dual-Color Fluorescence Nanoscopy Enabled by a Triplet-State Mechanism of Primed Conversion. *Angew Chem Int Ed Engl* **2017**, *56* (38), 11628–11633. https://doi.org/10.1002/anie.201706121.

4.   McEvoy, A. L.; Hoi, H.; Bates, M.; Platonova, E.; Cranfill, P. J.; Baird, M. A.; Davidson, M. W.; Ewers, H.; Liphardt, J.; Campbell, R. E. MMaple: A Photoconvertible Fluorescent Protein for Use in Multiple Imaging Modalities. *PLOS ONE* **2012**, *7* (12), e51314. https://doi.org/10.1371/journal.pone.0051314.

5.   Moeyaert, B.; Nguyen Bich, N.; De Zitter, E.; Rocha, S.; Clays, K.; Mizuno, H.; van Meervelt, L.; Hofkens, J.; Dedecker, P. Green-to-Red Photoconvertible Dronpa Mutant for Multimodal Super-Resolution Fluorescence Microscopy. *ACS Nano* **2014**, *8* (2), 1664–1673. https://doi.org/10.1021/nn4060144.

6.   Hertel, F.; Mo, G. C. H.; Duwé, S.; Dedecker, P.; Zhang, J. RefSOFI for Mapping Nanoscale Organization of Protein-Protein Interactions in Living Cells. *Cell Rep* **2016**, *14* (2), 390–400. https://doi.org/10.1016/j.celrep.2015.12.036.

7.   Hoi, H.; Matsuda, T.; Nagai, T.; Campbell, R. E. Highlightable Ca2+ Indicators for Live Cell Imaging. *J Am Chem Soc* **2013**, *135* (1), 46–49. https://doi.org/10.1021/ja310184a.

8.   Alieva, N. O.; Konzen, K. A.; Field, S. F.; Meleshkevitch, E. A.; Hunt, M. E.; Beltran-Ramirez, V.; Miller, D. J.; Wiedenmann, J.; Salih, A.; Matz, M. V. Diversity and Evolution of Coral Fluorescent Proteins. *PLOS ONE* **2008**, *3* (7), e2680. https://doi.org/10.1371/journal.pone.0002680.

9.   Ugalde, J. A.; Chang, B. S. W.; Matz, M. V. Evolution of Coral Pigments Recreated. *Science* **2004**, *305* (5689), 1433. https://doi.org/10.1126/science.1099597.

10.   Field, S. F.; Matz, M. V. Retracing Evolution of Red Fluorescence in GFP-Like Proteins from Faviina Corals. *Mol Biol Evol* **2010**, *27* (2), 225–233. https://doi.org/10.1093/molbev/msp230.

11.   Kim, H.; Grunkemeyer, T. J.; Modi, C.; Chen, L.; Fromme, R.; Matz, M. V.; Wachter, R. M. Acid–Base Catalysis and Crystal Structures of a Least Evolved Ancestral GFP-like Protein Undergoing Green-to-Red Photoconversion. *Biochemistry* **2013**, *52* (45), 8048–8059. https://doi.org/10.1021/bi401000e.

12. Kim, H.; Zou, T.; Modi, C.; Dörner, K.; Grunkemeyer, T. J.; Chen, L.; Fromme, R.; Matz, M. V.; Ozkan, S. B.; Wachter, R. M. A Hinge Migration Mechanism Unlocks the Evolution of Green-to-Red Photoconversion in GFP-like Proteins. *Structure* **2015**, *23* (1), 34–43. https://doi.org/10.1016/j.str.2014.11.011.

13. Krueger, T. D.; Tang, L.; Zhu, L.; Breen, I. L.; Wachter, R. M.; Fang, C. Dual Illumination Enhances Transformation of an Engineered Green-to-Red Photoconvertible Fluorescent Protein. *Angewandte Chemie* **2020**, *132* (4), 1661–1669. https://doi.org/10.1002/ange.201911379.

14. Pouwels, L. J.; Zhang, L.; Chan, N. H.; Dorrestein, P. C.; Wachter, R. M. Kinetic Isotope Effect Studies on the de Novo Rate of Chromophore Formation in Fast- and Slow-Maturing GFP Variants [†]. *Biochemistry* **2008**, *47* (38), 10111–10122. https://doi.org/10.1021/bi8007164.

15. Wachter, R. M. Photoconvertible Fluorescent Proteins and the Role of Dynamics in Protein Evolution. *Int J Mol Sci* **2017**, *18* (8). https://doi.org/10.3390/ijms18081792.

16. Tsutsui, H.; Shimizu, H.; Mizuno, H.; Nukina, N.; Furuta, T.; Miyawaki, A. The E1 Mechanism in Photo-Induced β-Elimination Reactions for Green-to-Red Conversion of Fluorescent Proteins. *Chemistry & Biology* **2009**, *16* (11), 1140–1147. https://doi.org/10.1016/j.chembiol.2009.10.010.

17. Lelimousin, M.; Adam, V.; Nienhaus, G. U.; Bourgeois, D.; Field, M. J. Photoconversion of the Fluorescent Protein EosFP: A Hybrid Potential Simulation Study Reveals Intersystem Crossings. *J. Am. Chem. Soc.* **2009**, *131* (46), 16814–16823. https://doi.org/10.1021/ja905380y.

18. Nienhaus, K.; Nienhaus, G. U.; Wiedenmann, J.; Nar, H. Structural Basis for Photo-Induced Protein Cleavage and Green-to-Red Conversion of Fluorescent Protein EosFP. *PNAS* **2005**, *102* (26), 9156–9159. https://doi.org/10.1073/pnas.0501874102.

19. Li, X.; Chung, L. W.; Mizuno, H.; Miyawaki, A.; Morokuma, K. Competitive Mechanistic Pathways for Green-to-Red Photoconversion in the Fluorescent Protein Kaede: A Computational Study. *J. Phys. Chem. B* **2010**, *114* (49), 16666–16675. https://doi.org/10.1021/jp1101779.

20. Fare, C.; Yuan, L.; Cordon-Preciado, V.; Michels, J. J.; Bearpark, M. J.; Rich, P.; van Thor, J. J. Radical-Triggered Reaction Mechanism of the Green-to-Red Photoconversion of EosFP. *J. Phys. Chem. B* **2020**, *124* (36), 7765–7778. https://doi.org/10.1021/acs.jpcb.0c04587.

CHAPTER 2

ELECTRON MICROSCOPY REVEALS SELF-ASSEMBLY AND COMPLEX

FORMATION IN SPINACH RUBISCO ACTIVASE

Abstract:

The AAA+ protein Rubisco activase (Rca) plays a critical role in the removal of inhibitors from the carbon-dioxide fixing enzyme Rubisco. Rubisco requires Rca regulation to recover its active site, which is prone to inhibition by regulatory molecules and misfire products. Present in plants, bacteria, and algae, these proteins perform a complicated set of behaviors which require substantial alterations to their structure. While the expression and behavior of Rca has been extensively studied, structural information has been difficult to obtain through classic biochemical techniques. The protein is known to form a vast variety of oligomeric assemblies dependent on the concentration and the presence of nucleotides and allosteric regulators. The relationship between structure and function is further complicated when Rubisco and Rca interact. The mechanism of reactivation remains unknown, although evidence suggests that Rca pulls a region of Rubisco polypeptide through its central pore to open its active site and release inhibitors.

Single-particle reconstruction using electron microscopy has become an available technique for investigation of the proteins, and both low- and high-resolution structures of bacterial Rubisco and Rca in complex have been obtained using negative-stain and cryo-electron microscopy (cryo-EM). We have investigated the structure of higher plant Rubisco activase from spinach, and its interactions with its cognate Rubisco, through negative-stain and cryo-EM experiments. While previous experiments have characterized

the trends in protein oligomerization, the higher-order arrangements in plant Rca have only been witnessed thus far in crystal structures.

We observed stable hexamers of the central (AAA+) domain of spinach Rca at a range of concentrations in the presence of ATP-γ-S, and cryo-EM allowed for the visualization of large arrangements which may function as inactive storage for the molecule. Unexpectedly, the protein self-associated into a variety of hexamer-based structures, including fibrils, 2D crystals, and 3D crystals. Negative stain of Rca and Rubisco revealed complexes similar to those from bacterial species, but a full 3D model has not been solved yet. We have shown that the AAA+ domain possesses the ability to form hexamers similar to WT protein with improved homogeneity. The diversity of higher-order structures displayed in our data indicates that a variety of organizational forms of Rca may form in vivo. As large oligomers have been shown to reduce activity, it is possible that these structures act as storage units to control levels of active Rca in the chloroplast. While it is known that concentration and nucleotide presence affect the degree of oligomerization, the introduction of multiple assembly types may indicate an additional form of regulation. Finally, the AAA+ domain of spinach Rca and cognate Rubisco do possess binding activity, and this interaction has been imaged using negative stain EM. Spinach Rca displays a side-on binding mode similar to that seen in bacterial Rca's. However, a high-resolution structure is needed to make a direct comparison and assess the specific interaction sites of the proteins.

Introduction:

1,5-ribulose bisphosphate carboxylase/oxygenase, or Rubisco, is responsible for the accumulation of biomass through CO2 fixation in autotrophic organisms and has been classified as the most abundant protein on the planet. The enzyme facilitates the carboxylation of the five-carbon sugar 1,5-ribulose bisphosphate (RuBP) prior to splitting the molecule into two 3-phosphoglycerate molecules as a part of the Calvin Cycle. The protein has a fairly strong affinity for CO2, but a relatively low k_{cat}. Previous *in vitro* experiments reported an average catalytic rate of 3 s^{-1} at 25°C, and an estimated *in vivo* average catalytic rate of ~0.03 s^{-1} for a single Rubisco enzyme on land [1]. Different forms of Rubisco (I, II, III, and IV) are distinguished through their phylogeny, quaternary structure, and catalytic function, with Form I being the most abundant [2]. Rubisco Forms II and III consist of dimers or multimers of large catalytic subunits (RbcL), while Form I Rubiscos, found in eukaryotes and bacteria, have a more complex hexadecameric structure with eight large subunits (RbcL) and eight small subunits (RbcS) [3]. Form I Rubiscos are divided into green- and red-type Rubiscos, which are both expressed in algae and bacteria, but plants only express the green-type Rubisco [2]. The site of carboxylation/oxygenation in all Rubisco enzymes is formed at the interface of two antiparallel RbcL units, which must be activated via carbamylation (carboxylation and
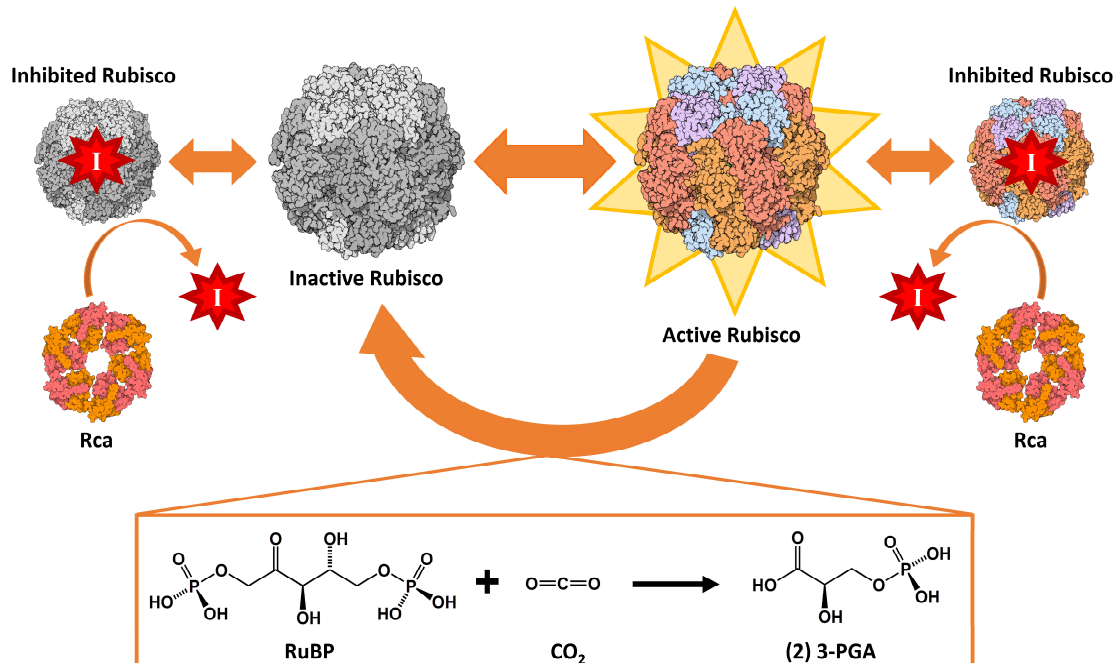
31

Figure 2.1. Rubisco cycles between catalysis, inactivation, and inhibition. Rubisco is activated through carbamylation, in which Mg^{2+} and CO_2 bind to the large subunits (shown in orange and red). Without carbamylation, Rubisco cannot perform carboxylation activity and CO_2 fixation will not occur. Both inactive and active forms can experience inhibition by binding a variety of sugar phosphates (I), which must be removed with the aid of the ATPase Rubisco activase (Rca, hexameric ring structure shown in red and orange).

Mg^{2+} binding) of a specific RbcL lysine residue before binding RuBP for a successful

carboxylation event (Fig. 2.1).

Rubisco struggles to distinguish between oxygen and CO_2, and more than a third

of all catalysis events result in the oxygenation of RuBP to phosphoglycolate, which is

unproductive in carbon fixation [4]. If RuBP encounters a de-carbamylated Rubisco or is

turned into XuBP (xylulose 1,5-bisphosphate) by a misfire reaction, it will occupy the

active site, preventing turnover. Other sugar-phosphate inhibitors have also been

discovered that stall Rubisco, and lengthy dialysis is insufficient to remove them from the

active site. Some inhibitors play a regulatory role, which may affect the stability and

resilience of plants and other organisms. For example, the naturally occurring tight-binding inhibitor CA1P (2-carboxyl-D-arabinitol 1-phosphate) is produced in the dark to regulate Rubisco activity through diurnal cycles and prevent unneeded energy expenditure. The regulatory function of these inhibitors relies on their intermittent removal, which allows for a controlled adjustment of Rubisco activity.

The enzyme responsible for inhibitor removal is Rubisco activase (Rca), which has evolved alongside Rubisco as its catalytic chaperone. A member of the AAA+ protein superfamily (ATPases Associated with diverse cellular Activities), Rca utilizes the energy from ATP hydrolysis to exert a mechanical function on Rubisco to promote inhibitor release. AAA+ proteins share a conserved domain containing a nucleotide-binding region adjacent to a catalytic module. They are typically hexameric and act on macromolecular substrates through their central pore [5]. Rca shares the same molecular architecture, with most solved structures exhibiting a hexameric structure.

Significant biochemical characterization of plant Rca has been performed since its discovery in the 1980s. Early on, genetic studies revealed that most plant species express two distinct isoforms of Rca either through separate genes or alternative splicing of mRNA, in roughly equal amounts. These separate isoforms are distinguished as longer (α) or shorter (β) isoforms, both containing an N-terminal domain essential for reactivation, and the former containing a C-terminal extension with redox-sensitive cysteines which may regulate activity [6, 7, 8, 9, 10]. While both isoforms have ATPase and reactivation activity, the purpose of two distinct isoforms is generally unknown. In certain plants, such as tobacco, only the shorter β-isoform is expressed, indicating that the presence of one isoform may be sufficient for reactivation [7].

Wild type (WT) and mutants of Rubisco activase, from plants and bacteria alike, have been tested for ATPase and reactivation activity as a function of concentration and nucleotide supplement [7, 8, 11, 12, 13,14]. The self-association of the protein is also highly dependent on these factors, and multiple experiments have demonstrated a clear positive correlation between concentration and multimer size, with very large oligomers lacking reactivation activity and combinations of dimers, tetramers, and hexamers possessing the highest activity rates [9, 11, 15, 16, 17]. The presence of nucleotides stabilizes protein assembly, but the relationship between oligomerization and nucleotide-binding state varies across species and isoform.

It has been established that Rca interacts with the large Rubisco subunit (RbcL) in higher plants, although the specific mode of interaction may be different across Form I Rubiscos [18]. Experiments utilizing hydrogen/deuterium exchange and electron microscopy (EM) have been utilized to characterize the binding between the red-type Rubisco and Rca [12, 14]. Such experiments have demonstrated that the red-type Rubiscos interact with Rca through the extended C-terminal domain of the large Rubisco subunit (RbcL), and the interaction is abolished when the outermost C-terminal residues are removed. In these systems, Rca binds in a side-on conformation, positioning its central pore of the hexamer over the C-terminal domain of the RbcL. The interaction between the surface of the hexamer and Rubisco is stabilized by helix α5 of the Rca AAA+ motif [14]. In contrast, the cryo-EM structure of a cyanobacterial Rubisco/Rca complex has revealed an alternative binding system, in which the N-terminal tail instead of the C-terminal tail of the RbcL interacts with Rca's central pore [8]. The discovery of this alternative binding mode raises the question of whether the red-type and green-type

34

Rubisco reactivation have fundamentally different reactivation mechanisms, and if there might be multiple reactivation mechanisms within the green-type Rubiscos.

The diversity in behavior among various isoforms indicates a highly regulated and specific system for reactivation which has evolved for different organisms. Although both self-association and Rubisco interaction have been examined through biochemical techniques, there is little structural information on the complexes and their arrangements in higher plants. To address the lack of structural details known about higher plant Rca, we have performed a study on the formations of spinach (*Spinacia oleracea*) Rubisco and Rca via negative-stain EM and cryo-EM. Stable hexamers of the Rca AAA+ domain were visualized in the presence of ATP-γ-S, and large organized fibrils and crystals were imaged under cryo-EM conditions. While no high-resolution three-dimensional (3D) structures were obtained from the data, the images provide a general structure for high-molecular-weight aggregates detected in previous studies. Interactions between spinach Rca and its cognate Rubisco were imaged under negative-stain EM, in which crosslinking was used to stabilize their interactions. Rca appeared to approach and bind Rubisco from the side, similar to bacterial Rca [8,14]. The binding of the AAA+ domain to Rubisco indicates that interface interactions involve this domain to a significant degree. However, a high-resolution 3D structure of the complex is needed to further evaluate the contacts between the two proteins. We have been using single-particle cryo-EM to probe the interactions in high-resolution cryo-EM data. Cryo-EM structures of Rca may be obtained by monitoring its individual hexamers using a carbon support or at conditions which promote high molecular weight structures. The procedures outlined here may

prove useful in imaging the cross-linked complex of Rubisco/Rca by single-particle cryo-EM.

Materials and Methods:

Plasmid design. The full-length α isoform (residues 1-416), β isoform (residues 1-378), and AAA+ region (residues 66-359) of spinach Rca were inserted into pHUE vectors, designed to attach a hexahistidine-tagged ubiquitin fusion protein to the N-terminus of the gene of interest. The full-length insert for SoαRca was synthesized and inserted at the NdeI and NotI restriction sites (BlueHeron Biotechnologies, Bothell, WA). The SoβRca and AAA+ region (SoαRca(66-239)) inserts were generated via PCR amplification from separate pET28(a+) plasmids containing the genes of interest by Nathan Henderson and BlueHeron Biotechnologies. Subsequent insertion into the vector using the SacII and NotI restriction sites was performed and the sequences of the resultant plasmids were verified at the DNA Shared Resource Facility at Arizona State University.

Expression and Purification. *Expression and Purification of SoαRca.* Chemically competent BL21(DE3) *E. coli* were transformed with the pHUE-SoαRca plasmid before selection on 100 µg/ml Carbenicillin LB agar plates. 6 L of liquid LB media containing 100 µg/ml Ampicillin were inoculated with single colonies and shaken at 250 rpm and 37°C until the culture reached exponential growth (OD_{600} of ~0.6), after which IPTG was added to a final concentration of 1 mM. Expression was allowed to proceed in the dark at 25°C and 200 rpm for 8 hours. Cells were then harvested by centrifugation at 4°C and suspended in a solution of 25 mM Tris-HCl (pH 8.0), 10 mM imidazole, 30% glycerol, 150 mM NaCl, 0.1 mM ethylenediaminetetraacetic acid

(EDTA), and 1 mM phenylmethylsulfonyl fluoride (PMSF). The slurry was sonicated and then centrifuged at 4°C. The supernatant was collected and filtered through 1.2-μm filters before being applied to a HisTrap HP nickel-nitrilotriacetic acid (Ni-NTA) column (GE Healthcare, Chicago, IL) using an ÄKTA pure FPLC system. A gradient of 92 mM to 500 mM imidazole was applied to the column for elution of the hexahistidine ubiquitin fusion protein. The protein was mixed with deubiquitinating enzyme and allowed to dialyze against 25 mM Tris-HCl (pH 8.0), 40 mM NaCl, 0.1 mM EDTA, 0.5 mM adenosine diphosphate (ADP) and 1 mM dithiothreitol (DTT). The protein was run over an additional HisTrap HP Ni-NTA column to separate the hexahistidine tag from the protein of interest. The sample pool was run over a Hi-Trap Q HP anion exchange column (GE Healthcare, Chicago, IL) and eluted with a linear gradient of 125 to 480 mM NaCl. The sample was buffer exchanged and concentrated into 25 mM HEPES (pH 7.5), 250 mM KCl, 5 mM $MgCl_2$, 10% glycerol, and 0.1 mM ATP-γ-S. Final protein concentration was determined from the absorbance at a wavelength of 280 nm ($\varepsilon = 28,880$ $M^{-1}cm^{-1}$) before flash freezing in liquid nitrogen and storage at -80°C.

Expression and Purification of SoβRca. Expression and purification of SoβRca was performed by Nathan Henderson. Chemically competent BL21(DE3) *E. coli* were transformed with the pHUE-SoβRca plasmid before selection in 100 μg/ml Carbenicillin LB liquid culture overnight. 6 L of liquid LB media containing 100 μg/ml Carbenicillin were inoculated with 5 ml of starter culture each and shaken at 250 rpm and 37°C for two hours before lowering the temperature to 30°C and continuing growth until the culture reached an OD_{600} of 0.55. The temperature was again lowered to 25°C and grown for 15 minutes to an OD_{600} of 0.65, after which IPTG was added to a final concentration of 1

37

mM. Expression was allowed to proceed in the dark at 25°C and 220 rpm for 8 hours. Cells were then harvested by centrifugation at 4°C and purification Protein was buffer exchanged and concentrated into either Buffer A) 50 mM HEPES (pH 7.5), 150 mM NaCl, and 1 mM DTT, or Buffer B) 50 mM HEPES (pH 7.5), 150 mM NaCl, 1 mM MnCl$_2$, and 1 mM ATP-γ-S. Final protein concentration was determined via Bradford assay before flash freezing in liquid nitrogen and storage at -80°C.

Expression and Purification of SoαRca(66-359). Expression and purification of SoαRca(66-359) was performed by Hoang Bui. Growth and purification steps described for SoαRca were followed. After purification, the protein was buffer exchanged and concentrated into 10 mM HEPES pH 7.5, 150 mM NaCl, 5 mM Mn^{2+}, 10% glycerol, and 0.5 mM ATP-γ-S. Final protein concentration was determined from A280 absorbance (ε = 28,880 M^{-1}cm^{-1}) before flash freezing in liquid nitrogen and storage at -80°C.

Expression and Purification of Spinach Rubisco. Expression and purification of spinach Rubisco were performed by Hoang Bui. Fresh spinach leaves were stored in the dark at 4°C before purification. 30 g of spinach leaves were combined with a 120 ml solution of 50 mM Tris-HCl (pH 8.0), 20 mM MgCl$_2$, 20 mM NaHCO$_3$, 0.2 mM EDTA, 1 mM PMSF, 5 mM DTT, 2% w/v polyvinylpolypyrrolidone (PVPP), and 1 protease inhibitor tablet (Roche). The homogenate was filtered through 2 layers of miracloth before centrifugation for 30 minutes at 4°C. The supernatant was precipitated with saturated ammonium sulfate and centrifuged to obtain a pellet. The pellet was resuspended in Rubisco isolation buffer composed of 25 mM Tris-HCl (pH 7.6), 10 mM MgCl$_2$, 10 mM NaHCO$_3$, 0.1 mM EDTA and 2 mM DTT. The solution was loaded onto a PD-10 desalting column (GE Healthcare) and eluted with Rubisco isolation buffer. The

protein was then run over a HiTrap Q HP column and eluted with a gradient of 120 mM to 500 mM KCl. Pooled fractions were filtered (0.22 μM) and concentrated before separation over a Superose 6 10/300 GL (GE Healthcare, Chicago, IL) and buffer exchanged into 25 mM Tris-HCl (pH 7.6), 10 mM $MgCl_2$, 10 mM $NaHCO_3$, 0.1 mM EDTA, 2 mM DTT, and 150 mM KCl. Protein was flash-frozen in liquid nitrogen and stored at -80°C.

Single-particle imaging in negative stain electron microscopy. Three different spinach Rca's were used to test for their stabilities of hexameric assemblies and their interaction with spinach Rubisco using negative-stain EM. The continuous-carbon-coated 400-mesh copper grids (PELCO #1GC400) were glow-discharged for 2 minutes before applying protein samples. The protein samples were then negatively stained with 2% uranyl acetate solution. A Tecnai F20 transmission electron microscope (TEM) and a Philips CM12 TEM were used to image the negatively stained protein samples at Arizona State University (ASU).

Protein constructs tested for stable hexamer formation. Full-length SoαRca was thawed on ice and serially diluted into 10 mM HEPES (pH 7.5), 150 mM NaCl, 2 mM ATP-γ-S, and 5 mM $MnCl_2$ to 76 and 38 nM monomer concentrations. Samples were negatively stained and imaged on a Philips CM 12 TEM. Mixtures of SoαRca and SoβRca were also negatively stained to evaluate for hexamer formation. These proteins were mixed in a 1:1 molar ratio of monomers to a final concentration of 284 μM. The protein mixture was diluted by a buffer of 10 mM HEPES (pH 7.5), 150 mM NaCl, 5 mM $MnCl_2$, and 2 mM nucleotide to a concentration of 36 nM monomer concentration before negative staining. Nucleotide conditions tested included 2 mM ATP-γ-S or a

mixture of 1 mM ATP and 1 mM ADP. Grids were imaged on a Philips CM 12 TEM. To screen the AAA+ domain (SoαRca(66-359)), the protein was diluted into a buffer solution of 10 mM HEPES (pH 7.5), 150 mM NaCl, 2 mM ATP-γ-S, and 5 mM MnCl$_2$ to monomer concentrations of 32 µM, 6.4 µM, 35 nM and 9 nM before negative staining. Grids were imaged on a Philips CM 12 TEM or a Tecnai F20 TEM.

Mixtures of Rca and Rubisco imaged via Negative Stain EM. The full-length SoαRca was tested for its natural affinity to spinach Rubisco through a negative stain experiment. Spinach Rubisco and SoαRca were diluted to 5 µM (hexadecamer) and 2 µM (hexamer) concentrations, respectively, into a buffer solution containing 20 mM HEPES (pH 7.5), 50 mM NaCl, 10 mM MgCl$_2$, 1 mM RuBP and 2 mM ATP-γ-S. The solution was allowed to incubate at room temperature for 1 minute before diluting to 8 µg ml^{-1} concentration for negative staining. Grids were imaged on a Tecnai F20 TEM.

Mixtures of spinach Rubisco and SoαRca(66-359) were imaged in the presence of 10 mM ATP-γ-S, ATP, and ADP to evaluate their effect on complex formation. Spinach Rubisco and SoαRca(66-359) were diluted to 5 µM (hexadecamer) and 2 µM (hexamer), respectively, into a buffer solution containing 20 mM HEPES (pH 7.5), 100 mM NaCl, 10 mM MgCl$_2$, 1 mM RuBP and 10 mM nucleotide. Nucleotides tested included ATP-γ-S, ATP, and ADP. A sample without nucleotide added was also produced. Samples were diluted to 8 µg ml^{-1} before negative staining and imaging on a Tecnai F20 TEM.

Carbamylated spinach Rubisco (ECM) was prepared by diluting to a 4 µM hexadecameric concentration in 20 mM HEPES (pH 7.5), 50 mM NaCl, 10 mM MgCl$_2$, 1 mM RuBP and 2 mM ATP-γ-S for one minute before adding NaHCO$_3$ to 40 mM concentration. After incubation for 8 minutes, SoαRca(66-359) was added to a final

hexameric concentration of 1 µM. The sample was diluted to a final concentration of 6 µg ml^{-1} before negative staining with 2% uranyl formate.

In order to stabilize SoαRca(66-359)-Rubisco complexes for negative stain imaging, a crosslinker was introduced to the solution. Crosslinked Rubisco-SoαRca(66-359) complexes (E-RuBP-Rca) were generated by mixing 5 µM Rubisco and 2 µM (hexamer) SoαRca(66-359) in a solution of 20 mM HEPES (pH 7.5), 50 mM NaCl, 10 mM MgCl$_2$, 1 mM RuBP, 2 mM ATP-γ-S, and 0.125% glutaraldehyde. The solution was diluted to a concentration of 7.5 µg ml^{-1} before negative staining with 2% uranyl formate.

A mixture of carbamylated Rubisco and Rca was crosslinked by combining 5 µM ECM with 2 µM hexameric SoαRca(66-359) and 0.125% glutaraldehyde for 10 minutes at room temperature. The protein solution was diluted to a final concentration of 6 µg ml^{-1} before negative staining with 2% uranyl formate. All grids were imaged on a Tecnai F20 TEM.

Single-particle cryo-EM imaging. *SoαRca(66-359) on holey carbon grids.* SoαRca(66-359) was diluted into 10 mM HEPES (pH 7.5), 150 mM NaCl, 2 mM ATPγS, and 5 mM MnCl$_2$ buffer to monomer concentrations of 1, 10, 22, 32 and 64 µM. Dilutions were applied to homemade holey carbon grids (produced by Dewight Williams) and plunge-frozen using a Vitrobot automatic plunge freezer at 4°C and 100% humidity, using a blot time of 6 s, a wait time of 1 s, and a blot pressure setting of 3 before viewing on a Tecnai F20 TEM.

SoαRca(66-359) on graphene-oxide-coated holey carbon grids. A glow-discharged C-Flat holey carbon grid (Cat# CF312-50) was rinsed with deionized water and coated with 0.2 mg/ml graphene oxide before wicking away the excess solution. 0.64

μM monomer concentration of protein (in 10 mM HEPES (pH 7.5), 150 mM NaCl, 2 mM ATPγS, and 5 mM MnCl$_2$) was applied to both sides of the grid before blotting for 6 s and plunging into liquid ethane using a manual plunge freezer. Grids were imaged on a Tecnai F20 TEM.

Crosslinking and Size Exclusion of Rca Hexamers. Glutaraldehyde crosslinking was performed to stabilize the hexameric protein for cryo-EM imaging. Protein was incubated at 32 μM monomer concentration in 10 mM HEPES (pH 7.5), 150 mM NaCl, 2 mM ATPγS, 5 mM MnCl$_2$, and 0.01% glutaraldehyde for ten minutes at before being run over a Superose 6 10/300 GL size exclusion column (GE Healthcare, Chicago, IL) equilibrated with 10 mM HEPES (pH 7.5), 150 mM NaCl, 5 mM MnCl$_2$, 100 μM ADP. Eluent was diluted to a subunit concentration of 0.245 μM (0.008 mg/ml) in 10 mM HEPES (pH 7.5), 150 mM NaCl, 5 mM MnCl$_2$, 2 mM ATP-γ-S for negative staining or hand plunge freezing on graphene oxide holey carbon grids. Negative stain grids were imaged on a Philips CM12 TEM, and frozen grids were imaged on a Tecnai F20 TEM.

Results:

SoαRca(66-359) is a stable truncated form of higher plant Rca. We evaluated a set of spinach Rubisco activase proteins for their tendency to form stable hexamers at concentrations appropriate for negative-stain EM. Full-length WT α and β isoforms, as well as the AAA+ module (SoαRca(66-359)) were imaged in the presence of nucleotide (ATP-γ-S, some tested with ATP or ADP) and Mn^{2+} to test their stability and affinity for hexamer formation at low (~35 nM) subunit concentrations. Subunit concentrations of ~30-40 nM resulted in a single layer of distinct particles deposited on the carbon surface. Toroidal oligomers were present in samples of full-length SoαRca (residues 1-413), full-
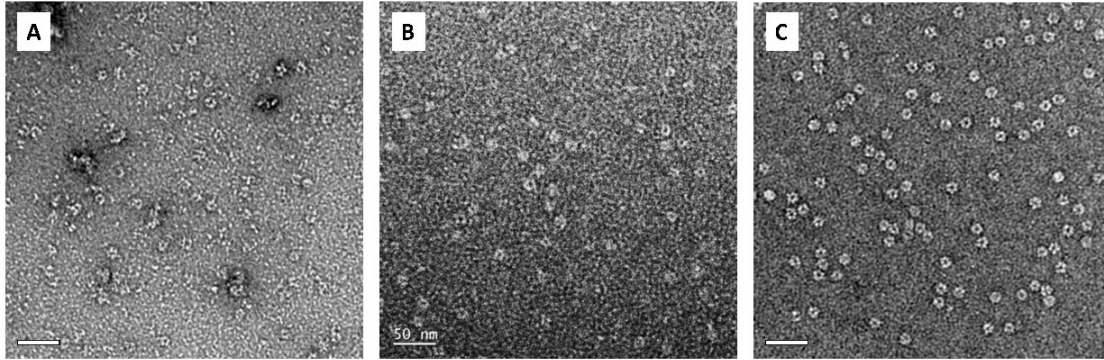
Figure 2.2. Electron images of the negatively stained Rca. A) Full length SoαRca, (B) a 1:1 mixture of SoαRca and SoβRca, and (C) SoαRca (66-359) are shown in the presence of 2 mM ATP-γ-S and 1 mM Mn^{2+}, imaged via negative-stain EM. Scale bars (white, lower left) are 50 nm.

length SoβRca (1-378), and the AAA+ domain (66-359) in the presence of ATP-γ-S (Fig. 2.2). In the presence of ATP-γ-S, SoαRca displayed a mixture of hexameric and amorphous protein, with monomers, dimers, hexamers and open toroids present throughout the sample. Loose, closed rings varied slightly in size and shape, but the quality of the images limited the numeration of monomers in each. A 1:1 mixture of SoαRca and SoβRca supplemented with ATP-γ-S produced irregular toroids similar to those of isolated SoαRca with less populated monomers and dimers. The mixture became fully amorphous in the presence of a 1:1 mixture of ATP:ADP. In the presence of ATP-γ-S, SoαRca(66-359) formed homogeneous hexamers roughly 10 nm in diameter, and the protein appeared to preferentially bind with the pore axis perpendicular to the carbon surface.

The AAA+ domain of Rca self-assembles into high-order oligomers. Thus far, cryo-EM studies have focused on the complex of Rubisco and Rca, whereas structures of Rca have been determined largely by crystallography and negative-stain EM [8,14,19, 20]. The proteins are well-packed into one state for crystallography to determine the

atomic positions at high resolutions, while EM allows for visualizing the proteins in the solutions, or native-like states, which contain different conformations and dynamic information. Because cryo-EM images are directly formed by the electron scattering of the protein and solvent molecules, one can use these molecular images to reconstruct a high-resolution 3D structure. Due to the dynamic and semi-flexible nature of Rca, we turned to cryo-EM to investigate the structure of the nucleotide-bound Rca. To visualize single hexamers and examine the concentration dependence via cryo-EM, SoαRca (66-359) was loaded onto a holey carbon grid and vitrified at a range of concentrations between 1 μM (0.03 mg/ml) to 64 μM (2.1 mg/ml) in the presence of 2 mM ATP-γ-S.

The AAA+ domain formed several distinct higher-order structures that changed quickly over a range of concentrations (Fig. 2.3). Stacks or helices of Rca were imaged at
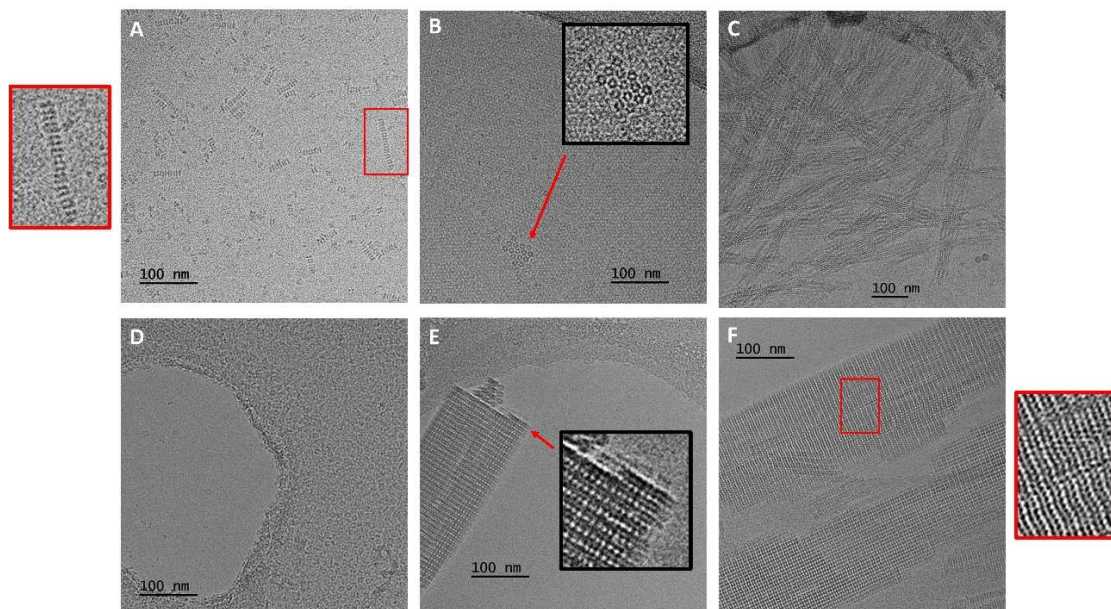

Figure 2.3. Cryo-EM images of the spinach Rca. The AAA+ domain of spinach Rubisco activase forms a variety of higher-order oligomers at a range of concentrations. Shown here are monomeric concentrations of (A) 64 μM, (B)32 μM, (C) 22 μM, (D) 10 μM, (E) and (F) 1 μM. Structural arrangements appear to be loosely concentration-dependent, with single hexamers or small crystals appearing at lower (<~10 μM) concentrations.

the highest tested concentration (2.1 mg/ml), with each hexamer measuring ~10 nm wide

with a ~4 nm pitch per helix turn. The number of hexamers per fibril varied between two

to ~30 hexamers. While the helical arrangements have been determined in the plant Rca

crystals and the higher quaternary structures have been indicated through other

characterization techniques, free self-assembled helices in solution have not been

identified [9, 12, 21]. Recent studies indicate that aggregates greater than six hexamers

accumulate between subunit concentrations of 10-100 μM, and that Rca at these

concentrations are not catalytically active, suggesting that higher structures may be used

to store inactive protein [11]. The images here provide a line of evidence of spontaneous

helical arrangement of the AAA+ domain in the presence of ATP-γ-S at a relatively high

(~2 mg/ml or ~64 μM subunit) protein concentration. This behavior is consistent with the

formation of fibrillar structures in the absence of RuBP as a storage mechanism. It should

be noted that these results have not been replicated, and the formation of these fibers may

be particularly sensitive to changes in concentration due to rapid dilution or specific grid

conditions.

A widespread two-dimensional (2D) crystal arrangement of SoαRca(66-359) was

imaged at 32 μM subunit concentration. A single or double layer of Rca was organized

into a homogeneous side-by-side packed arrangement of 200×200 nm or larger. A 2D

crystal projection was reconstructed by Po-Lin Chiu using the FOCUS software [22]. The

crystal lattice was indexed as a = 104.5 Å, b = 104.5 Å, and γ = 60°, and the crystal

structure had a plane group of *p*6 (phase error: 35.2°) (Fig. 2.4). Fourier filtering and

lattice unbending were employed to reach at 4 Å resolution in the 2D projection map. The

map confirms that the hexamer is formed in the 2D crystal array. When compared to a

model of tobacco Rca (containing residues 68-383) obtained by fitting a crystal structure into negative-stain EM density, the structures appear to match, but the width of the hexamer and pore size of SoαRca (66-359) are significantly smaller [9]. Our 2D
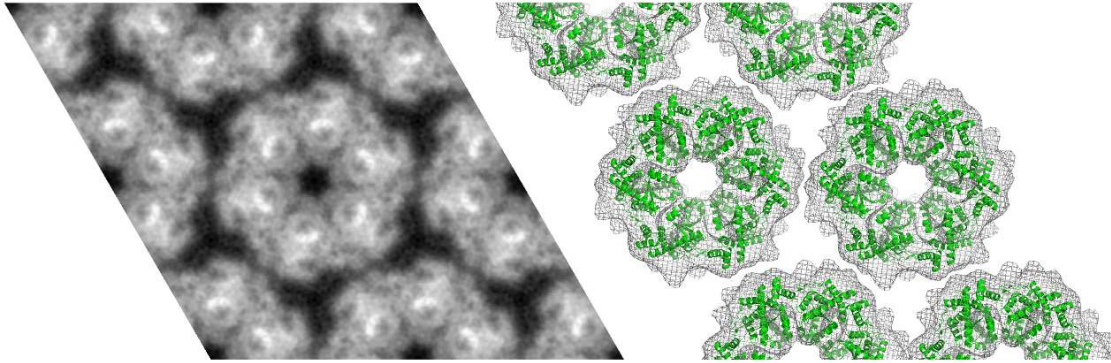

Figure 2.4. Left: A projection of the 2D crystals formed by SoαRca (66-359) at ~32 μM subunit concentration, courtesy of Po-Lin Chiu. Rca appears to form flat, closed hexamers in this crystal formation. Right: A hexameric model of tobacco Rca (lacking the 67-residue N-domain), fit into a negative stain EM density of tobacco Rca(R294V) [9].

projection shows hexamers with an outer diameter of ~100 Å and a ~15 Å pore. Their hexameric model is ~125 Å wide with a pore width of ~30 Å, while the EM density is 135 Å in diameter with a 36 Å pore. The size discrepancy may be due to the structural deformation resulting from the negative staining procedure for preparing tobacco Rca. Another possibility could be due to a combination of fewer residues (~22 less than ΔN68) and a more densely packed crystal. This result was unexpected, because the SoαRca (66-359) crystals were formed very quickly in solution, without high concentration or precipitants to encourage the growth of a tightly packed crystal. Although a 3D structure has not yet been accessible from our projection of Rca, our results prove that highly regular crystals can be formed spontaneously by the protein which may serve a function *in vivo*. Further single-particle cryo-EM or a MicroED approach could be used to resolve these questions.

46

Lower concentrations exhibited Rca's high affinity for the carbon support, and a majority of protein below 20-30 µM concentration could be found stuck to the carbon surface. The protein also collected in disorganized aggregates, possibly formed from several helical fibers, between 22-64 µM concentrations. At 1 µM concentration, tightly packed submicron microcrystals were formed which seem to be made of helical structures with a similar (~4 nm) inter-particle distance from center to center. Previously reported aggregates consisting of >12 hexamers could consist of bundled aggregates, fibers, or crystals, but it is unknown if this diverse set of arrangements serve a biological function.

SoαRca(66-359) displayed a high affinity for carbon support, and efforts to vitrify single hexamers in holey grids were unsuccessful. Graphene oxide coatings were employed to capture isolated hexamers for cryo-EM imaging. Subunit concentrations of 0.64 and 0.064 µM were deposited and vitrified on graphene oxide coated holey carbon grids before viewing in cryo-EM conditions on a Tecnai F20 TEM. Initial screenings indicated that the protein did not adhere well to the graphene oxide grids, appearing heterogeneous and denatured. Proteins were cross-linked with glutaraldehyde and run over a size exclusion column to isolate stabilized hexamers before viewing under the negative-stain and cryo-EM conditions (Fig. 2.5). Two peaks were observed in the size-exclusion chromatographic profile. The first peak fraction contained hexameric crosslinked Rca, while the second was composed of smaller oligomers, likely a combination of randomly crosslinked and non-crosslinked subunits. Although a high

concentration of homogeneous hexamers was imaged under negative stain conditions on continuous carbon grids, the same sample applied to graphene-oxide-coated holey carbon grids in cryo-EM conditions appeared heterogeneous, and low particle density was viewed.
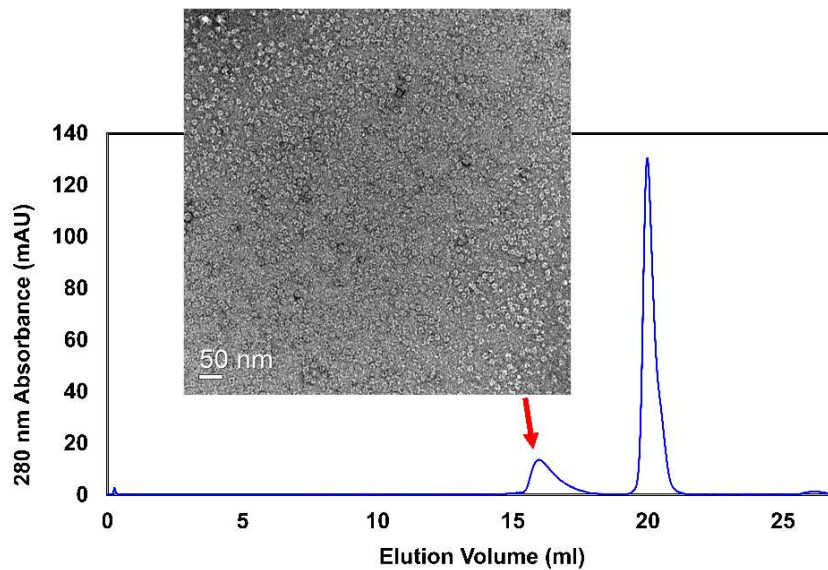

Figure 2.5. SoαRca (66-359) was crosslinked and run over a size exclusion column to isolate the hexameric form of the protein for cryo-EM studies. The chromatogram shown here shows the 280 absorbance after injection (~0 ml), the elution peaks of crosslinked hexamers (at ~16 ml) and smaller oligomers (at ~20 ml). A negative-stain EM image of crosslinked hexamers is shown with a scale bar of 50 nm.

Spinach Rca exhibits a "side-on" binding orientation to endogenous Rubisco.

SoαRca with spinach Rubisco. Full-length SoαRca was mixed with Rubisco in the presence of ATP-γ-S and RuBP. A few Rubisco-Rca complexes were observed, exhibiting a familiar side-on binding orientation seen in bacterial Rca's (Fig. 2.6). However, a majority of the protein population was of separate Rubisco or Rca. SoαRca otherwise formed low-molecular-weight, polydisperse forms, including sub-hexameric oligomers and monomers. A particle population of the dimers of hexamers was present in

48

the solution as well. The lack of isolated hexamers suggests that when not bound to Rubisco or another Rca hexamer, the subunits tend to fall apart.

SoαRca(66-359) with spinach Rubisco. The AAA+ domain was imaged in conjunction with Rubisco to examine the behavior of binding under various nucleotide conditions. The AAA+ domain (SoαRca(66-359)) was combined with Rubisco in the presence of RuBP and a saturating concentration of ATP, ADP, or ATP-γ-S (Fig. 2.7). A few Rubisco-Rca complexes could be seen on samples containing 10 mM ATP; however, a large majority of the protein was isolated. Rca appeared mostly polydisperse, forming
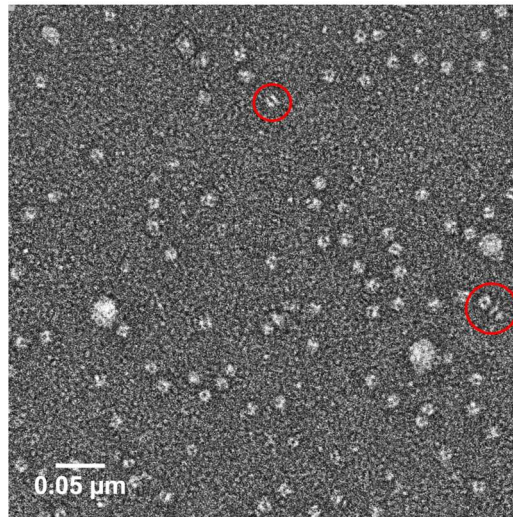
Figure 2.6. Electron image of negatively-stained full-length SoαRca with spinach Rubisco in the presence of ATP-γ-S. Hexamers are seen which form dodecamers (red circle, top center) and attach in a side-on fashion to Rubisco (red circle, right of center). Small subunits (~1-5 nm) are scattered throughout the sample. Scale bar (bottom left) is 50 nm.

oligomers between monomer-hexamer, as well as dodecamers containing ~2 stacked or helical hexamers. Aggregates of several monomers in large ring shapes between 20-30 nm in diameter were unique to this condition. In the presence of ADP, no Rubisco-Rca

complexes were observed. A large particle distribution of Rca was observed here, with the protein ranging from monomeric to dodecameric states. In the presence of ATP-γ-S, hexamers, and stacks/helices of hexamers between 2-6 units were observed, as well as some monomers. However, no Rubisco-Rca complexes were observed. When no nucleotide was included in the mixture, Rca was extremely polydisperse, forming broken
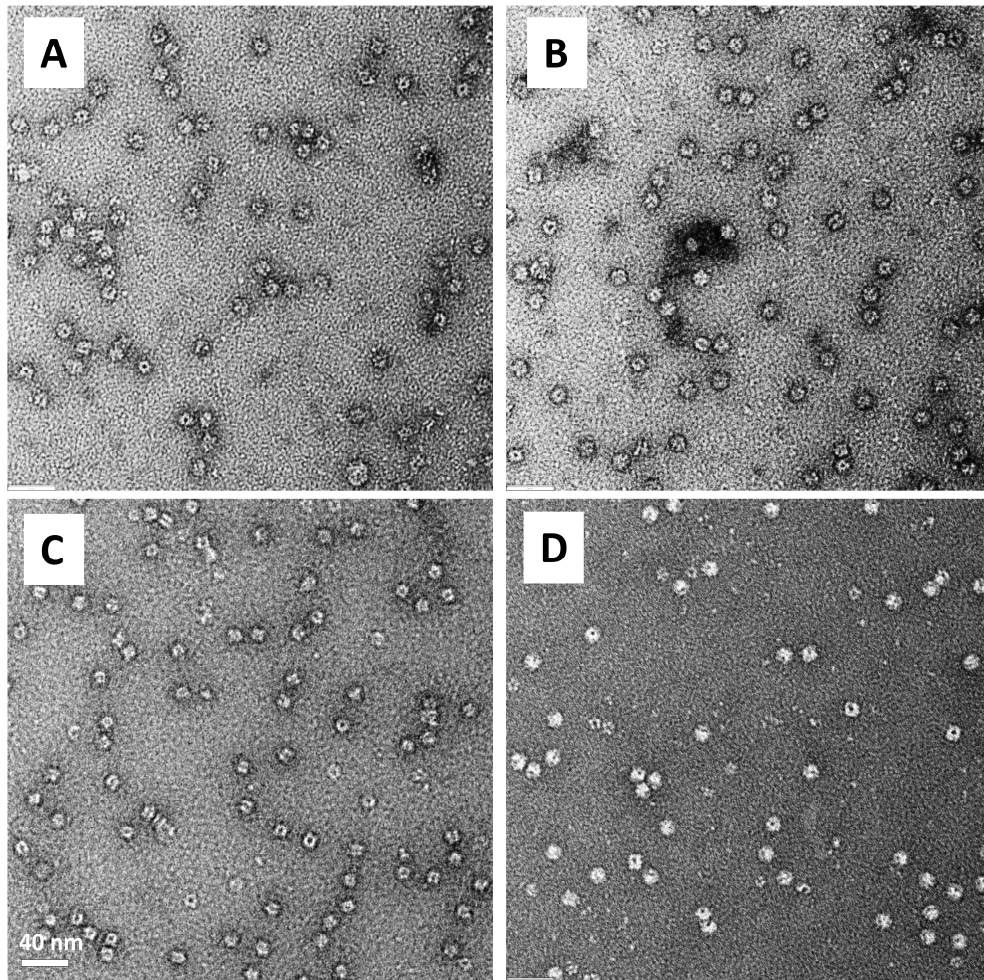

Figure 2.7. Negative-stain EM images of SoαRca(66-359) and spinach Rubisco with (A) ATP, (B) ADP, (C) ATP-γ-S and (D) without nucleotide. No Rubisco-Rca complexes were imaged under these conditions, but various forms of Rca can be seen, in hexameric stacks or helices (C) and in various stages of disassembly (D). Scale bar (bottom left) is 40 nm.

or irregular hexameric and pentameric rings, aggregates between 1-4 monomers, and a small amount of dodecamers (Fig. 2.7).

To capture any transient interactions between the two proteins, crosslinking was employed. Stable hexamers of the AAA+ domain had been observed in the presence of ATP-γ-S, both in isolation and in the presence of Rubisco, so this construct was used to examine hexamer-hexadecamer associations between Rubisco and Rca. After crosslinking at 0.125% glutaraldehyde in the presence of ATP-γ-S and RuBP, complexes exhibiting a side-on binding mode of Rca to Rubisco were imaged (Fig. 2.8, Panel A). Hexamers were otherwise found mostly in dodecameric form, however, and a majority of the Rubisco and Rca populations were not crosslinked to each other.
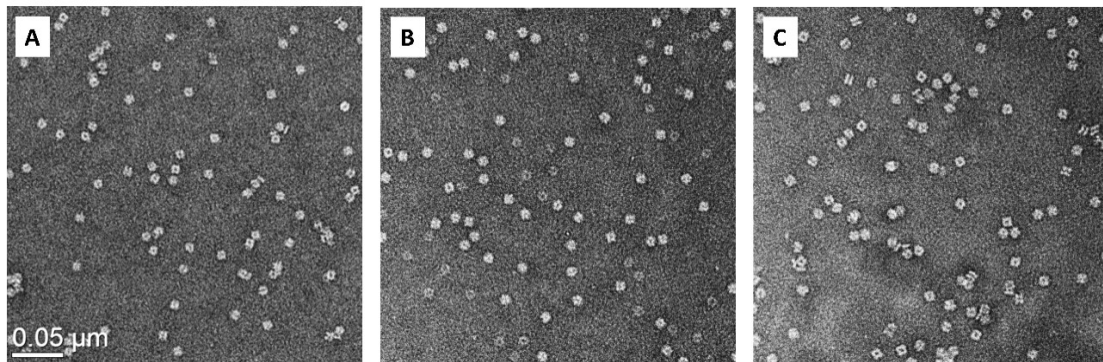
Figure 2.8. (A) Rubisco: SoαRca(66-359) complexes were stabilized via glutaraldehyde crosslinking. Complexes exhibit a side-on conformation and appear to prefer an orientation in which the side-view of the Rca hexamer and a top-view of Rubisco can be seen. (B) Carbamylated spinach Rubisco and Rca appeared to form no stable complexes, unless crosslinked with glutaraldehyde (C). Crosslinking also appeared to stabilize the dodecameric stacked or helical form of Rca.

Rubisco was carbamylated through the addition of 40 mM $NaHCO_3$ and 5 mM Mg^{2+} before incubation with RuBP and addition of SoαRca(66-359) (Fig. 2.8, Panel B). Negative stain EM of the solution indicated no complex formation, but after a crosslinking step was introduced, Rubisco-Rca complexes were resolved (Fig. 2.8, Panel

C). A similar amount of interactions was captured under these conditions to those of crosslinked de-carbamylated Rubisco and Rca. Instances of one or two Rca hexamers binding to Rubisco were imaged. Although RuBP was supplied in the mixture, no inhibitors for activated Rubisco were present. Even so, carbamylation appeared to have no negative effect on transient interactions between Rubisco and Rca.

Discussion and Conclusion:

Rca is responsible for maintaining the omnipresent Rubisco, and therefore plays a vital role in the cycle of carbon through the ecosystem. It is known to be a dynamic protein capable of subunit exchange and rapid oligomerization dependent on concentration and nucleotide presence [11, 16, 23]. It has been postulated that the hexameric form of Rca is the active form, however, it makes up only a portion of the multimeric possibilities, with the protein generating multimers >6 subunits which are catalytically inactive [11, 13]. While Rca hexamers may be the main multimeric species to interact with Rubisco [12, 14], it is unlikely that the protein maintains this form for long, as recent studies support a dynamic activation cycle involving various oligomeric states and rapid subunit exchange [11, 23].

While protein dynamics and association can be studied in the lab, spectroscopically or otherwise, this behavior causes limitations in gaining important structural information. Thus far, the higher plant Rca structures include those of tobacco, creosote bush, and Arabidopsis thaliana, but many structures lack detail on the C- and N-termini due to their flexibility [9, 17, 21]. We have sought to use negative-stain and cryo-EM to characterize the homogeneity and behavior of spinach Rca isoforms. In particular,

we have examined the AAA+ domain of spinach Rca with an interest in its role in hexamer formation, nucleotide-binding function, and substrate binding function.

In spinach, two different isoforms of Rubisco activase are expressed as a result of alternative pre-mRNA splicing [24]. Both contain an identical 65-residue N terminal domain and a central 293-residue AAA+ domain essential for activity. Their sequences differ only in their C-terminal domain, which is 37 residues longer in the 45 kDa α-isoform than the 41 kDa β-isoform. While both are generally expressed in equal amounts and both exhibit ATPase and reactivation activity, they possess different biophysical characteristics. The α isoform has higher thermostability and is available for redox regulation through two C-terminal cysteines [25], while the β isoform in spinach has a higher reactivation rate [26]. While these behaviors have been well-documented, their structural consequences are not well-understood. We have used negative stain EM to examine recombinantly expressed α and β isoforms of spinach rubisco activase, as well as a mutant containing only the AAA+ (residues 66-359) domain. The constructs were imaged in the presence of the slowly-hydrolyzing ATP-γ-S (~38-fold slower than ATP hydrolysis by spinach β Rca), which has been shown to stabilize hexamers and reduce subunit exchange in spinach Rca [23]. The assembling of both full-length proteins appears to be aggregated and some polydispersity at the nanomolar subunit concentrations was visualized by negative-stain EM. ATP-γ-S does improve the homogeneity of the α and β isoforms in comparison to ATP /ADP mixtures. However, the AAA+ domain construct in the presence of ATP-γ-S appeared to form the most homogeneous selection of hexamers of the three constructs. While the N- terminus is necessary for full reactivation capability, and the C-terminus plays a regulatory role, they

are often left out in crystallographic studies due to their flexibility [7, 9, 27]. It is possible

that the AAA+ domain's rigidity, and lack of regulatory residues, allows for hexamers to

accumulate and prevents the protein's tendency towards dispersion.

We aimed to characterize the AAA+ domain through single particle cryo-EM;

however, the stable hexamers imaged under negative stain EM conditions were not

responsive to cryo-EM conditions. Low concentrations of protein led to the high

aggregation of disorganized hexamers onto the surface of the carbon scaffold. The high

affinity of Rca for the carbon film led us to explore using graphene oxide as a support

layer. Unfortunately, few particles were attracted to the graphene oxide, and they

appeared heterogeneous, even after hexamer crosslinking and isolation via SEC.

Despite difficulties with imaging individual Rca hexamers, large organized

aggregates were seen in cryo-EM conditions at high subunit concentrations of the protein

between 1-64 µM. Fibrils extending from ~2 to ~30 hexamers were imaged at the highest

concentration tested, while 2D and 3D crystalline structures were imaged between 1-32

µM concentrations. Our findings complement multiple studies which have described the

aggregation of higher plant Rca into large multimers at high concentrations. While

nucleotides shift the average size of multimer present, both ATP-γ-S, ATP/ADP mixtures

and isolated ADP can promote a broad range of higher order oligomers [9, 11, 23, 26].

Crystals formed from both plant and bacterial Rubisco activase tend to form hexameric or

helical structures with ~6 monomers per turn, which have indicated possible forms for

activity and storage [9, 17]. While the helical fibers of other AAA+ proteins have been

visualized using negative-stain EM, the images of higher plant Rca fibrils and crystals

shown here are novel. Although previous studies have measured the average molecular

weight or number of subunits per large aggregate formed in high concentration conditions, the relative arrangement of subunits was unknown. The helical arrangements with six subunits per turn have been proposed based on plant Rca crystal structures with the same arrangement, and here we provide evidence that they form in solution at high concentrations. However, the presence of other high molecular weight arrangements at lower concentrations adds another level of complexity to Rca self-assembly. A simple model in which subunits are procedurally added on to a growing helix may be accurate under certain conditions, but large aggregates may also compose themselves into 2D or 3D crystals of varying heights, widths, or depths.

In an effort to better characterize the complex formed between plant Rubisco and Rca, we purified spinach Rubisco and combined it with full-length and truncated SoαRa for imaging via negative stain EM. SoαRca(66-359) was imaged with Rubisco in the presence of ATP, ADP, or ATP-γ-S, under the theory that ATP-γ-S would stabilize the Rubisco-Rca complex. However, while nucleotide presence did change the oligomerization behavior of Rca, it did not appear to affect the complex formation and no Rubisco-Rca complexes were imaged. Full-length SoαRa, however, formed complexes with Rubisco in the presence of ATP-γ-S and RuBP. Both SoαRa and the AAA+ domain showed complex formation when crosslinker (glutaraldehyde) was applied. Because the AAA+ domain required crosslinking for complexes to be captured, the full-length protein may have a higher affinity for Rubisco. This is consistent with the idea that the N-terminal domain of Rca contains residues that are vital for interaction and reactivation of Rubisco [7, 8]. However, the striking side-on attachment of the full-length and AAA+ hexamers to Rubisco is highly similar to complexes observed for the purple bacterium

Rhodobacter sphaeroides and cyanobacterium Nostoc, which points to a somewhat stable interaction between both protein forms and Rubisco [8, 14].

Carbamylation did not abolish the interaction between Rubisco and Rca as expected. When Rubisco is activated via carbamylation without the presence of an inhibitor, Rca ideally has no interaction with the protein. However, under these conditions Rubisco and Rca formed complexes similar to those seen with de-carbamylated Rubisco. Because RuBP was present in the mixture active turnover within the solution may result in inhibited complexes of EM-RuBP or ECM-XuBP, which may cause the recruitment of Rca. However, it is possible that Rubisco and Rca still interact when Rubisco is in its active form. The higher amount of available CO_2 appeared to influence the assembly of Rca, which formed dodecamers in the presence of 40 mM $NaHCO_3$.

Negative stain and cryo-EM have been used in recent decades to discover novel structures and behaviors in plant Rca. While it has proven difficult to view plant Rca as a functional hexamer in cryo-EM conditions, its behaviors at high concentrations and in mixture with Rubisco may offer another route to structural information. Here we have shown that high molecular weight aggregates can be visualized by cryo-EM, which has been successfully used to image bacterial Rubisco/Rca complexes. We have not attempted to induce large aggregates under a different nucleotide composition or with the full-length isoforms of spinach Rca, and such experiments may provide stable arrangements for 3D structure determination through cryo-EM or Micro-ED techniques. Spinach Rubisco-Rca complexes should be imaged under cryo-EM conditions and evaluated for 3D structure determination, as a high-resolution structure of a plant

Rubisco/Rca complex has not been solved to date. While the high-resolution structures of

plant Rca's are still sought after, the images provided here of high molecular weight

aggregates and Rubisco/Rca complexes can offer some insight into the self-assembly

behaviors and reactivation mechanism of plant Rca.

References:

1. Bar-On, Y. M.; Milo, R. The Global Mass and Average Rate of Rubisco. *Proc Natl Acad Sci U S A* **2019**, *116* (10), 4738–4743. https://doi.org/10.1073/pnas.1816654116.

2. Tabita, F. R.; Satagopan, S.; Hanson, T. E.; Kreel, N. E.; Scott, S. S. Distinct Form I, II, III, and IV Rubisco Proteins from the Three Kingdoms of Life Provide Clues about Rubisco Evolution and Structure/Function Relationships. *J Exp Bot* **2008**, *59* (7), 1515–1524. https://doi.org/10.1093/jxb/erm361.

3. Bracher, A.; Whitney, S. M.; Hartl, F. U.; Hayer-Hartl, M. Biogenesis and Metabolic Maintenance of Rubisco. *Annu. Rev. Plant Biol.* **2017**, *68* (1), 29–60. https://doi.org/10.1146/annurev-arplant-043015-111633.

4. Peterhansel, C.; Krause, K.; Braun, H.-P.; Espie, G. S.; Fernie, A. R.; Hanson, D. T.; Keech, O.; Maurino, V. G.; Mielewczik, M.; Sage, R. F. Engineering Photorespiration: Current State and Future Possibilities. *Plant Biol (Stuttg)* **2013**, *15* (4), 754–758. https://doi.org/10.1111/j.1438-8677.2012.00681.x.

5. Puchades, C.; Sandate, C. R.; Lander, G. C. The Molecular Principles Governing the Activity and Functional Diversity of AAA+ Proteins. *Nature Reviews Molecular Cell Biology* **2020**, *21* (1), 43–58. https://doi.org/10.1038/s41580-019-0183-6.

6. Zhang, N.; Portis, A. R. Mechanism of Light Regulation of Rubisco: A Specific Role for the Larger Rubisco Activase Isoform Involving Reductive Activation by Thioredoxin-f. *PNAS* **1999**, *96* (16), 9438–9443. https://doi.org/10.1073/pnas.96.16.9438.

7. Esau, B. D.; Snyder, G. W.; Portis, A. R. Differential Effects of N- and C-Terminal Deletions on the Two Activities of Rubisco Activase. *Arch Biochem Biophys* **1996**, *326* (1), 100–105. https://doi.org/10.1006/abbi.1996.0052.

8. Flecken, M.; Wang, H.; Popilka, L.; Hartl, F. U.; Bracher, A.; Hayer-Hartl, M. Dual Functions of a Rubisco Activase in Metabolic Repair and Recruitment to Carboxysomes. *Cell* **2020**, *183* (2), 457-473.e20.

https://doi.org/10.1016/j.cell.2020.09.010.

9. Stotz, M.; Mueller-Cajar, O.; Ciniawsky, S.; Wendler, P.; Hartl, F. U.; Bracher, A.; Hayer-Hartl, M. Structure of Green-Type Rubisco Activase from Tobacco. *Nat Struct Mol Biol* **2011**, *18* (12), 1366–1370. https://doi.org/10.1038/nsmb.2171.

10. Esau, B. D.; Snyder, G. W.; Portis Jr, A. R. Activation of Ribulose-1,5-Bisphosphate Carboxylase/Oxygenase (Rubisco) with Chimeric Activase Proteins. *Photosynthesis Research* **1998**, *58* (2), 175–181. https://doi.org/10.1023/A:1006133212261.

11. Serban, A. J.; Breen, I. L.; Bui, H. Q.; Levitus, M.; Wachter, R. M. Assembly-Disassembly Is Coupled to the ATPase Cycle of Tobacco Rubisco Activase. *J Biol Chem* **2018**, *293* (50), 19451–19465. https://doi.org/10.1074/jbc.RA118.005047.

12. Mueller-Cajar, O.; Stotz, M.; Wendler, P.; Hartl, F. U.; Bracher, A.; Hayer-Hartl, M. Structure and Function of the AAA+ Protein CbbX, a Red-Type Rubisco Activase. *Nature* **2011**, *479* (7372), 194–199. https://doi.org/10.1038/nature10568.

13. Barta, C.; Dunkle, A. M.; Wachter, R. M.; Salvucci, M. E. Structural Changes Associated with the Acute Thermal Instability of Rubisco Activase. *Arch Biochem Biophys* **2010**, *499* (1–2), 17–25. https://doi.org/10.1016/j.abb.2010.04.022.

14. Bhat, J. Y.; Miličić, G.; Thieulin-Pardo, G.; Bracher, A.; Maxwell, A.; Ciniawsky, S.; Mueller-Cajar, O.; Engen, J. R.; Hartl, F. U.; Wendler, P.; Hayer-Hartl, M. Mechanism of Enzyme Repair by the AAA+ Chaperone Rubisco Activase. *Mol Cell* **2017**, *67* (5), 744-756.e6. https://doi.org/10.1016/j.molcel.2017.07.004.

15. Chakraborty, M.; Kuriata, A. M.; Nathan Henderson, J.; Salvucci, M. E.; Wachter, R. M.; Levitus, M. Protein Oligomerization Monitored by Fluorescence Fluctuation Spectroscopy: Self-Assembly of Rubisco Activase. *Biophysical Journal* **2012**, *103* (5), 949–958. https://doi.org/10.1016/j.bpj.2012.07.034.

16. Kuriata, A. M.; Chakraborty, M.; Henderson, J. N.; Hazra, S.; Serban, A. J.; Pham, T. V. T.; Levitus, M.; Wachter, R. M. ATP and Magnesium Promote Cotton Short-Form Ribulose-1,5-Bisphosphate Carboxylase/Oxygenase (Rubisco) Activase Hexamer Formation at Low Micromolar Concentrations. *Biochemistry* **2014**, *53* (46), 7232–7246. https://doi.org/10.1021/bi500968h.

17. Henderson, J. N.; Hazra, S.; Dunkle, A. M.; Salvucci, M. E.; Wachter, R. M. Biophysical Characterization of Higher Plant Rubisco Activase. *Biochimica et Biophysica Acta (BBA) - Proteins and Proteomics* **2013**, *1834* (1), 87–97. https://doi.org/10.1016/j.bbapap.2012.09.006.

18. Wachter, R. M.; Salvucci, M. E.; Carmo-Silva, A. E.; Barta, C.; Genkov, T.; Spreitzer, R. J. Activation of Interspecies-Hybrid Rubisco Enzymes to Assess Different Models for the Rubisco–Rubisco Activase Interaction. *Photosynth Res* **2013**, *117* (1), 557–566. https://doi.org/10.1007/s11120-013-9827-0.

19. Tsai, Y.-C. C.; Ye, F.; Liew, L.; Liu, D.; Bhushan, S.; Gao, Y.-G.; Mueller-Cajar, O. Insights into the Mechanism and Regulation of the CbbQO-Type Rubisco Activase, a MoxR AAA+ ATPase. *PNAS* **2020**, *117* (1), 381–387. https://doi.org/10.1073/pnas.1911123117.

20. Henderson, J. N.; Kuriata, A. M.; Fromme, R.; Salvucci, M. E.; Wachter, R. M. Atomic Resolution X-Ray Structure of the Substrate Recognition Domain of Higher Plant Ribulose-Bisphosphate Carboxylase/Oxygenase (Rubisco) Activase. *J Biol Chem* **2011**, *286* (41), 35683–35688. https://doi.org/10.1074/jbc.C111.289595.

21. Hasse, D.; Larsson, A. M.; Andersson, I. Structure of Arabidopsis Thaliana Rubisco Activase. *Acta Crystallogr D Biol Crystallogr* **2015**, *71* (Pt 4), 800–808. https://doi.org/10.1107/S1399004715001182.

22. Biyani, N.; Righetto, R. D.; McLeod, R.; Caujolle-Bert, D.; Castano-Diez, D.; Goldie, K. N.; Stahlberg, H. Focus: The Interface between Data Collection and Data Processing in Cryo-EM. *J Struct Biol* **2017**, *198* (2), 124–133. https://doi.org/10.1016/j.jsb.2017.03.007.

23. Peterson-Forbrook, D. S.; Hilton, M. T.; Tichacek, L.; Henderson, J. N.; Bui, H. Q.; Wachter, R. M. Nucleotide Dependence of Subunit Rearrangements in Short-Form Rubisco Activase from Spinach. *Biochemistry* **2017**, *56* (36), 4906–4921. https://doi.org/10.1021/acs.biochem.7b00574.

24. Werneke, J. M.; Chatfield, J. M.; Ogren, W. L. Alternative MRNA Splicing Generates the Two Ribulosebisphosphate Carboxylase/Oxygenase Activase Polypeptides in Spinach and Arabidopsis. *Plant Cell* **1989**, *1* (8), 815–825. https://doi.org/10.1105/tpc.1.8.815.

25. Crafts-Brandner, S. J.; Van De Loo, F. J.; Salvucci, M. E. The Two Forms of Ribulose-1,5-Bisphosphate Carboxylase/Oxygenase Activase Differ in Sensitivity to Elevated Temperature. *Plant Physiol* **1997**, *114* (2), 439–444.

26. Keown, J. R.; Pearce, F. G. Characterization of Spinach Ribulose-1,5-Bisphosphate Carboxylase/Oxygenase Activase Isoforms Reveals Hexameric Assemblies with Increased Thermal Stability. *Biochem J* **2014**, *464* (3), 413–423. https://doi.org/10.1042/BJ20140676.

27. Shivhare, D.; Ng, J.; Tsai, Y.-C. C.; Mueller-Cajar, O. Probing the Rice Rubisco–Rubisco Activase Interaction via Subunit Heterooligomerization. *PNAS* **2019**, *116* (48), 24041–24048. https://doi.org/10.1073/pnas.1914245116.

REFERENCES

CHAPTER 1

1. Schmidt, A.; Wiesner, B.; Schülein, R.; Teichmann, A. Use of Kaede and Kikume Green-Red Fusions for Live Cell Imaging of G Protein-Coupled Receptors. *Methods Mol Biol* **2014**, *1174*, 139–156. https://doi.org/10.1007/978-1-4939-0944-5_9.

2. Hilderbrand, S. A.; Weissleder, R. Near-Infrared Fluorescence: Application to in Vivo Molecular Imaging. *Curr Opin Chem Biol* **2010**, *14* (1), 71–79. https://doi.org/10.1016/j.cbpa.2009.09.029.

3. Ma, M.; Ay, K.; Lr, S.; K, N.; Cj, O.; J, L.-S.; Gu, N.; P, P. Rational Engineering of Photoconvertible Fluorescent Proteins for Dual-Color Fluorescence Nanoscopy Enabled by a Triplet-State Mechanism of Primed Conversion. *Angew Chem Int Ed Engl* **2017**, *56* (38), 11628–11633. https://doi.org/10.1002/anie.201706121.

4. McEvoy, A. L.; Hoi, H.; Bates, M.; Platonova, E.; Cranfill, P. J.; Baird, M. A.; Davidson, M. W.; Ewers, H.; Liphardt, J.; Campbell, R. E. MMaple: A Photoconvertible Fluorescent Protein for Use in Multiple Imaging Modalities. *PLOS ONE* **2012**, *7* (12), e51314. https://doi.org/10.1371/journal.pone.0051314.

5. Moeyaert, B.; Nguyen Bich, N.; De Zitter, E.; Rocha, S.; Clays, K.; Mizuno, H.; van Meervelt, L.; Hofkens, J.; Dedecker, P. Green-to-Red Photoconvertible Dronpa Mutant for Multimodal Super-Resolution Fluorescence Microscopy. *ACS Nano* **2014**, *8* (2), 1664–1673. https://doi.org/10.1021/nn4060144.

6. Hertel, F.; Mo, G. C. H.; Duwé, S.; Dedecker, P.; Zhang, J. RefSOFI for Mapping Nanoscale Organization of Protein-Protein Interactions in Living Cells. *Cell Rep* **2016**, *14* (2), 390–400. https://doi.org/10.1016/j.celrep.2015.12.036.

7. Hoi, H.; Matsuda, T.; Nagai, T.; Campbell, R. E. Highlightable Ca2+ Indicators for Live Cell Imaging. *J Am Chem Soc* **2013**, *135* (1), 46–49. https://doi.org/10.1021/ja310184a.

8. Alieva, N. O.; Konzen, K. A.; Field, S. F.; Meleshkevitch, E. A.; Hunt, M. E.; Beltran-Ramirez, V.; Miller, D. J.; Wiedenmann, J.; Salih, A.; Matz, M. V. Diversity and Evolution of Coral Fluorescent Proteins. *PLOS ONE* **2008**, *3* (7), e2680. https://doi.org/10.1371/journal.pone.0002680.

9. Ugalde, J. A.; Chang, B. S. W.; Matz, M. V. Evolution of Coral Pigments Recreated. *Science* **2004**, *305* (5689), 1433. https://doi.org/10.1126/science.1099597.

10. Field, S. F.; Matz, M. V. Retracing Evolution of Red Fluorescence in GFP-Like

Proteins from Faviina Corals. *Mol Biol Evol* **2010**, *27* (2), 225–233. https://doi.org/10.1093/molbev/msp230.

11. Kim, H.; Grunkemeyer, T. J.; Modi, C.; Chen, L.; Fromme, R.; Matz, M. V.; Wachter, R. M. Acid–Base Catalysis and Crystal Structures of a Least Evolved Ancestral GFP-like Protein Undergoing Green-to-Red Photoconversion. *Biochemistry* **2013**, *52* (45), 8048–8059. https://doi.org/10.1021/bi401000e.

12. Kim, H.; Zou, T.; Modi, C.; Dörner, K.; Grunkemeyer, T. J.; Chen, L.; Fromme, R.; Matz, M. V.; Ozkan, S. B.; Wachter, R. M. A Hinge Migration Mechanism Unlocks the Evolution of Green-to-Red Photoconversion in GFP-like Proteins. *Structure* **2015**, *23* (1), 34–43. https://doi.org/10.1016/j.str.2014.11.011.

13. Krueger, T. D.; Tang, L.; Zhu, L.; Breen, I. L.; Wachter, R. M.; Fang, C. Dual Illumination Enhances Transformation of an Engineered Green-to-Red Photoconvertible Fluorescent Protein. *Angewandte Chemie* **2020**, *132* (4), 1661–1669. https://doi.org/10.1002/ange.201911379.

14. Pouwels, L. J.; Zhang, L.; Chan, N. H.; Dorrestein, P. C.; Wachter, R. M. Kinetic Isotope Effect Studies on the de Novo Rate of Chromophore Formation in Fast- and Slow-Maturing GFP Variants [†]. *Biochemistry* **2008**, *47* (38), 10111–10122. https://doi.org/10.1021/bi8007164.

15. Wachter, R. M. Photoconvertible Fluorescent Proteins and the Role of Dynamics in Protein Evolution. *Int J Mol Sci* **2017**, *18* (8). https://doi.org/10.3390/ijms18081792.

16. Tsutsui, H.; Shimizu, H.; Mizuno, H.; Nukina, N.; Furuta, T.; Miyawaki, A. The E1 Mechanism in Photo-Induced β-Elimination Reactions for Green-to-Red Conversion of Fluorescent Proteins. *Chemistry & Biology* **2009**, *16* (11), 1140–1147. https://doi.org/10.1016/j.chembiol.2009.10.010.

17. Lelimousin, M.; Adam, V.; Nienhaus, G. U.; Bourgeois, D.; Field, M. J. Photoconversion of the Fluorescent Protein EosFP: A Hybrid Potential Simulation Study Reveals Intersystem Crossings. *J. Am. Chem. Soc.* **2009**, *131* (46), 16814–16823. https://doi.org/10.1021/ja905380y.

18. Nienhaus, K.; Nienhaus, G. U.; Wiedenmann, J.; Nar, H. Structural Basis for Photo-Induced Protein Cleavage and Green-to-Red Conversion of Fluorescent Protein EosFP. *PNAS* **2005**, *102* (26), 9156–9159. https://doi.org/10.1073/pnas.0501874102.

19. Li, X.; Chung, L. W.; Mizuno, H.; Miyawaki, A.; Morokuma, K. Competitive Mechanistic Pathways for Green-to-Red Photoconversion in the Fluorescent Protein Kaede: A Computational Study. *J. Phys. Chem. B* **2010**, *114* (49), 16666–16675. https://doi.org/10.1021/jp1101779.

20. Fare, C.; Yuan, L.; Cordon-Preciado, V.; Michels, J. J.; Bearpark, M. J.; Rich, P.; van Thor, J. J. Radical-Triggered Reaction Mechanism of the Green-to-Red Photoconversion of EosFP. *J. Phys. Chem. B* **2020**, *124* (36), 7765–7778. https://doi.org/10.1021/acs.jpcb.0c04587.

CHAPTER 2

1. Bar-On, Y. M.; Milo, R. The Global Mass and Average Rate of Rubisco. *Proc Natl Acad Sci U S A* **2019**, *116* (10), 4738–4743. https://doi.org/10.1073/pnas.1816654116.

2. Tabita, F. R.; Satagopan, S.; Hanson, T. E.; Kreel, N. E.; Scott, S. S. Distinct Form I, II, III, and IV Rubisco Proteins from the Three Kingdoms of Life Provide Clues about Rubisco Evolution and Structure/Function Relationships. *J Exp Bot* **2008**, *59* (7), 1515–1524. https://doi.org/10.1093/jxb/erm361.

3. Bracher, A.; Whitney, S. M.; Hartl, F. U.; Hayer-Hartl, M. Biogenesis and Metabolic Maintenance of Rubisco. *Annu. Rev. Plant Biol.* **2017**, *68* (1), 29–60. https://doi.org/10.1146/annurev-arplant-043015-111633.

4. Peterhansel, C.; Krause, K.; Braun, H.-P.; Espie, G. S.; Fernie, A. R.; Hanson, D. T.; Keech, O.; Maurino, V. G.; Mielewczik, M.; Sage, R. F. Engineering Photorespiration: Current State and Future Possibilities. *Plant Biol (Stuttg)* **2013**, *15* (4), 754–758. https://doi.org/10.1111/j.1438-8677.2012.00681.x.

5. Puchades, C.; Sandate, C. R.; Lander, G. C. The Molecular Principles Governing the Activity and Functional Diversity of AAA+ Proteins. *Nature Reviews Molecular Cell Biology* **2020**, *21* (1), 43–58. https://doi.org/10.1038/s41580-019-0183-6.

6. Zhang, N.; Portis, A. R. Mechanism of Light Regulation of Rubisco: A Specific Role for the Larger Rubisco Activase Isoform Involving Reductive Activation by Thioredoxin-f. *PNAS* **1999**, *96* (16), 9438–9443. https://doi.org/10.1073/pnas.96.16.9438.

7. Esau, B. D.; Snyder, G. W.; Portis, A. R. Differential Effects of N- and C-Terminal Deletions on the Two Activities of Rubisco Activase. *Arch Biochem Biophys* **1996**, *326* (1), 100–105. https://doi.org/10.1006/abbi.1996.0052.

8. Flecken, M.; Wang, H.; Popilka, L.; Hartl, F. U.; Bracher, A.; Hayer-Hartl, M. Dual Functions of a Rubisco Activase in Metabolic Repair and Recruitment to Carboxysomes. *Cell* **2020**, *183* (2), 457-473.e20. https://doi.org/10.1016/j.cell.2020.09.010.

9. Stotz, M.; Mueller-Cajar, O.; Ciniawsky, S.; Wendler, P.; Hartl, F. U.; Bracher, A.; Hayer-Hartl, M. Structure of Green-Type Rubisco Activase from Tobacco. *Nat Struct Mol Biol* **2011**, *18* (12), 1366–1370. https://doi.org/10.1038/nsmb.2171.

10. Esau, B. D.; Snyder, G. W.; Portis Jr, A. R. Activation of Ribulose-1,5-Bisphosphate Carboxylase/Oxygenase (Rubisco) with Chimeric Activase Proteins. *Photosynthesis Research* **1998**, *58* (2), 175–181. https://doi.org/10.1023/A:1006133212261.

11. Serban, A. J.; Breen, I. L.; Bui, H. Q.; Levitus, M.; Wachter, R. M. Assembly-Disassembly Is Coupled to the ATPase Cycle of Tobacco Rubisco Activase. *J Biol Chem* **2018**, *293* (50), 19451–19465. https://doi.org/10.1074/jbc.RA118.005047.

12. Mueller-Cajar, O.; Stotz, M.; Wendler, P.; Hartl, F. U.; Bracher, A.; Hayer-Hartl, M. Structure and Function of the AAA+ Protein CbbX, a Red-Type Rubisco Activase. *Nature* **2011**, *479* (7372), 194–199. https://doi.org/10.1038/nature10568.

13. Barta, C.; Dunkle, A. M.; Wachter, R. M.; Salvucci, M. E. Structural Changes Associated with the Acute Thermal Instability of Rubisco Activase. *Arch Biochem Biophys* **2010**, *499* (1–2), 17–25. https://doi.org/10.1016/j.abb.2010.04.022.

14. Bhat, J. Y.; Miličić, G.; Thieulin-Pardo, G.; Bracher, A.; Maxwell, A.; Ciniawsky, S.; Mueller-Cajar, O.; Engen, J. R.; Hartl, F. U.; Wendler, P.; Hayer-Hartl, M. Mechanism of Enzyme Repair by the AAA+ Chaperone Rubisco Activase. *Mol Cell* **2017**, *67* (5), 744-756.e6. https://doi.org/10.1016/j.molcel.2017.07.004.

15. Chakraborty, M.; Kuriata, A. M.; Nathan Henderson, J.; Salvucci, M. E.; Wachter, R. M.; Levitus, M. Protein Oligomerization Monitored by Fluorescence Fluctuation Spectroscopy: Self-Assembly of Rubisco Activase. *Biophysical Journal* **2012**, *103* (5), 949–958. https://doi.org/10.1016/j.bpj.2012.07.034.

16. Kuriata, A. M.; Chakraborty, M.; Henderson, J. N.; Hazra, S.; Serban, A. J.; Pham, T. V. T.; Levitus, M.; Wachter, R. M. ATP and Magnesium Promote Cotton Short-Form Ribulose-1,5-Bisphosphate Carboxylase/Oxygenase (Rubisco) Activase Hexamer Formation at Low Micromolar Concentrations. *Biochemistry* **2014**, *53* (46), 7232–7246. https://doi.org/10.1021/bi500968h.

17. Henderson, J. N.; Hazra, S.; Dunkle, A. M.; Salvucci, M. E.; Wachter, R. M. Biophysical Characterization of Higher Plant Rubisco Activase. *Biochimica et Biophysica Acta (BBA) - Proteins and Proteomics* **2013**, *1834* (1), 87–97. https://doi.org/10.1016/j.bbapap.2012.09.006.

18. Wachter, R. M.; Salvucci, M. E.; Carmo-Silva, A. E.; Barta, C.; Genkov, T.; Spreitzer, R. J. Activation of Interspecies-Hybrid Rubisco Enzymes to Assess Different Models for the Rubisco–Rubisco Activase Interaction. *Photosynth Res* **2013**, *117* (1), 557–566. https://doi.org/10.1007/s11120-013-9827-0.

19. Tsai, Y.-C. C.; Ye, F.; Liew, L.; Liu, D.; Bhushan, S.; Gao, Y.-G.; Mueller-Cajar, O. Insights into the Mechanism and Regulation of the CbbQO-Type Rubisco Activase, a MoxR AAA+ ATPase. *PNAS* **2020**, *117* (1), 381–387. https://doi.org/10.1073/pnas.1911123117.

20. Henderson, J. N.; Kuriata, A. M.; Fromme, R.; Salvucci, M. E.; Wachter, R. M. Atomic Resolution X-Ray Structure of the Substrate Recognition Domain of Higher Plant Ribulose-Bisphosphate Carboxylase/Oxygenase (Rubisco) Activase. *J Biol Chem* **2011**, *286* (41), 35683–35688. https://doi.org/10.1074/jbc.C111.289595.

21. Hasse, D.; Larsson, A. M.; Andersson, I. Structure of Arabidopsis Thaliana Rubisco Activase. *Acta Crystallogr D Biol Crystallogr* **2015**, *71* (Pt 4), 800–808. https://doi.org/10.1107/S1399004715001182.

22. Biyani, N.; Righetto, R. D.; McLeod, R.; Caujolle-Bert, D.; Castano-Diez, D.; Goldie, K. N.; Stahlberg, H. Focus: The Interface between Data Collection and Data Processing in Cryo-EM. *J Struct Biol* **2017**, *198* (2), 124–133. https://doi.org/10.1016/j.jsb.2017.03.007.

23. Peterson-Forbrook, D. S.; Hilton, M. T.; Tichacek, L.; Henderson, J. N.; Bui, H. Q.; Wachter, R. M. Nucleotide Dependence of Subunit Rearrangements in Short-Form Rubisco Activase from Spinach. *Biochemistry* **2017**, *56* (36), 4906–4921. https://doi.org/10.1021/acs.biochem.7b00574.

24. Werneke, J. M.; Chatfield, J. M.; Ogren, W. L. Alternative MRNA Splicing Generates the Two Ribulosebisphosphate Carboxylase/Oxygenase Activase Polypeptides in Spinach and Arabidopsis. *Plant Cell* **1989**, *1* (8), 815–825. https://doi.org/10.1105/tpc.1.8.815.

25. Crafts-Brandner, S. J.; Van De Loo, F. J.; Salvucci, M. E. The Two Forms of Ribulose-1,5-Bisphosphate Carboxylase/Oxygenase Activase Differ in Sensitivity to Elevated Temperature. *Plant Physiol* **1997**, *114* (2), 439–444.

26. Keown, J. R.; Pearce, F. G. Characterization of Spinach Ribulose-1,5-Bisphosphate Carboxylase/Oxygenase Activase Isoforms Reveals Hexameric Assemblies with Increased Thermal Stability. *Biochem J* **2014**, *464* (3), 413–423. https://doi.org/10.1042/BJ20140676.

27. Shivhare, D.; Ng, J.; Tsai, Y.-C. C.; Mueller-Cajar, O. Probing the Rice Rubisco–Rubisco Activase Interaction via Subunit Heterooligomerization. *PNAS* **2019**, *116* (48), 24041–24048. https://doi.org/10.1073/pnas.1914245116.